This is a repository copy of *Particle transport in turbulent square duct flows with a free surface*.

White Rose Research Online URL for this paper:
https://eprints.whiterose.ac.uk/208581/

Version: Accepted Version

Particle transport in turbulent square duct flows with a free surface

Yanzhi Wang[1] (王艳芝), Lee F. Mortimer[2], Michael Fairweather[2], Wenli Ma[1] (马文礼),
Yanzhong Zhen[1] (甄延忠)

[1]*Research Center of Efficient Exploitation of Oil and Gas Resources and Protection Ecological Environment, Universities of Shaanxi Province, School of Petroleum Engineering and Environmental Engineering, Yan'an University, Yan'an 716000, China*
[2] *School of Chemical and Process Engineering, University of Leeds, Leeds, LS2 9JT, UK*

ABSTRACT

Direct numerical simulation combined with a one-way coupled Lagrangian particle tracking technique is employed to investigate dilute particle-laden turbulent flows in open square ducts with a free surface. The focus is on examining the influence of the mean cross-stream secondary flow on particle transport near the wall, free surface, and across the duct cross section. Based on the duct half-width and mean friction velocity, a shear Reynolds number of $Re_\tau = 300$ is considered, with the corresponding particle Stokes numbers ranging from $St^+ = 0.31$ to 260. The results reveal that particle concentration near the sidewalls is lower than that near the bottom wall, and the minimum particle concentration is observed at the free surface. Along the bottom wall centerline orientated upwards, particle concentration gradually decreases. An exception to this is in the vicinity of the free surface where a slight increase is observed for the heavier particles ($St^+ \geqslant 25$), and the amplitude of this increase gradually declines as the Stokes number increases. In the streamwise direction near the free surface, heavier particles tend to preferentially concentrate in regions where the instantaneous transverse secondary flow velocity is negative. As the Stokes number increases, the position of the maximum streamwise velocity for heavier particles is closer to the free surface, and the rotation centres of inner and outer secondary particle motions gradually disappear. The streamwise root mean square velocity for the lightest $St^+ = 0.31$ particles is higher than that for particles with higher inertia in the middle region of the free surface.

I. INTRODUCTION

Particle-laden flows in turbulent open ducts are encountered in various practical applications[1-3], with sediment transport and dispersion of floaters on the open free surface of rivers being one of the most prevalent examples. A distinguishing characteristic of these flows is the presence of secondary flows arising from the anisotropy of turbulence[4-6], which manifests due to two key phenomena of open ducts: the interactions between the turbulence and two solid walls in the corner regions, and the interaction between sidewall turbulence and the free surface at the

junction of the mixed boundary.

Previous studies pertaining to the secondary flows in the corner region of closed square ducts [7-10] have been widely conducted. It was found that a pair of secondary flow vortices exists in the duct corner regions. They are positioned symmetrically about the corner bisector and can transfer fluid momentum from the central region of the duct to the corner areas, thereby exerting a significant influence on the mean flow statistics. Moreover, particle-laden flows in turbulent closed square ducts have been extensively investigated, and the secondary flows were further demonstrated to play a crucial role in the motion of particles embedded within the flow. Winkler *et al.* [11] first reported that the deposition of low-inertia particles in a vertical turbulent square duct is more pronounced than that observed in circular pipe flows due to the presence of secondary flows. Phares and Sharma [12] additionally highlighted that the secondary flows enhance the deposition of high-inertia particles in the duct corner regions while suppressing the deposition of low-inertia particles in the same area. These findings were subsequently confirmed by Yao and Fairweather [13] who extended the investigations to a higher Reynolds number and concluded that the influence of secondary flows on particle deposition exhibits a strong dependence on the Reynolds number. Noorani *et al.* [14] examined the effect of aspect ratio on particle transport in turbulent duct flows and found that the impact of secondary flows on mean particle concentration, velocity, and their fluctuations is highly sensitive to particle inertia. In a recent study, Lin *et al.* [15] investigated the modulation of turbulence by neutrally buoyant particles in a turbulent square duct and observed that the secondary flows are intensified, with their centres of rotation shifting closer to the central region of the duct cross-section. Fornari *et al.* [16] further demonstrated that the modulation effect of neutrally buoyant particles on the secondary flows depends on the particle volume fraction $\emptyset_V$. The intensity of the secondary flow was observed to be enhanced when $\emptyset_V \leq 0.1$, while above this critical value, the turbulence and secondary motions were reduced in strength. More recently, Wang *et al.* [17] analyzed the preferential concentration of inertial particles in a square duct with a dilute particle-laden flow. Their results indicated that particle accumulation near the corner regions is dominated by the secondary flows, whereas particle preferential concentration in the wall-central area is predominantly governed by the coherent structures in the buffer layer.

In contrast, the secondary flows in turbulent open ducts exhibit patterns distinct from those of closed duct flows[4], and this difference is primarily attributable to the presence of a free surface. The main feature of turbulence near the free surface is the redistribution of turbulence intensities, while the secondary flows in the mixed-boundary corners, formed by the solid wall and free surface of the open duct, can facilitate the transfer of fluid momentum from the sidewall to the free surface. Grega *et al.* [18] studied the transport mechanism of turbulent flow along a mixed-boundary corner and successfully identified the inner and outer secondary flow which were found to transport low-momentum

fluid towards the free surface, thereby thickening the boundary layer in its vicinity. Sreedhar and Stern [19] conducted simulations of turbulent flow in a developing mixed-boundary juncture between a solid wall and a rigid lid. Their results indicate that the mean turbulent flow field in the juncture is significantly altered by the mean secondary flows within this region. Furthermore, it was observed that the turbulence kinetic energy increases as the rigid-lid boundary is approached, where it is redistributed from the surface-normal direction to the other two coordinate directions. These observations were corroborated by Roglia et al. [5] in their large eddy simulations of turbulent flows in open square ducts, where they additionally reported that the mean friction velocity along the duct sidewalls first increases and then decreases as the free surface is approached, owing to the convection of inner secondary flows in the mixed-boundary corner regions. Kang and Choi [20] also made similar observations in their simulation of turbulent flow in a rectangular open channel. Sakai and Uhlmann [21] examined the origins of mean secondary motions in fully developed turbulence within an open duct, and concluded that the pattern, size and location of the inner secondary flow vortices exhibits a strong dependence on Reynolds number. Nikitin [22] proposed that the formation of secondary flows near the free surface in open duct flow is linked to the distribution of local flow pressure, with the secondary flow reaching 5% of the bulk velocity magnitude on the free surface, a value significantly larger than that observed in closed duct flows. Nevertheless, there are limited detailed studies on particle-laden flows in open ducts.

The previous studies predominantly focused attention on investigating the interaction between near-wall turbulence and particle behaviour in particle-laden open channel flows [23-25], where the flow in the spanwise direction is assumed to be homogeneous, thus the effect of secondary flows can be ignored. Concerning the effect of free-surface turbulence, Haarlem et al. [26] examined particle deposition onto a free surface in an open channel flow and observed a preferential accumulation of particles in ribbon-like structures along the edges of large, roughly circular regions near the free surface. In these regions, particle motions are subjected to the large-scale vortices of free-surface turbulence. These observations were later confirmed in the work of Narayanan et al. [23]. Lovecchio et al. [27] investigated the dispersion of floater particles in a turbulent shear-free surface of an open channel flow and noted that light particles tend to cluster, forming filamentary structures in regions of local compression caused by the downwelling of free-surface turbulence. However, the influence of secondary flows on particle distribution near the free surface was not considered in these studies. In contrast, Kundu and Ghoshal [28] emphasized the significant role played by cross-sectional secondary flows in the concentration distribution of suspended sediment in open channel flows, particularly in channels with small aspect ratios. Wang et al. [29] conducted simulations of particle dispersion in high Reynolds number open square duct flows, considering the effect of secondary flows and particle gravity. Their findings revealed that the secondary flows tend to encourage lower inertia particles to concentrate in the central area

of bottom wall and higher inertia particles to accumulate in the lower corner regions of the duct, which resembles particle behaviour observed in closed duct flows. However, particles in open duct flows exhibit less dispersion compared to closed duct flows due to the influence of the free surface. In conclusion, the mechanisms of particle transport in turbulent open square duct flows remain unclear, and further research to comprehensively investigate the effects of secondary flows and free-surface turbulence is necessary.

To the authors' knowledge, the present study is the first direct numerical simulation of fully turbulent particle-laden flow in an open square duct with a top free surface. The chosen shear Reynolds number is Re_τ=300, based on the duct half-width and mean friction velocity, with a wide range of shear Stokes number St^+=0.31~260 considered. The focus of this work is to investigate the effects of the secondary flows induced by the interaction of wall turbulence and free-surface turbulence on particle transport in open square duct flows. The paper is organized as follows: In Sec. II, the numerical model and methodology employed for both the fluid and particulate phases are presented. Sec. III.A provides a brief discussion of the results obtained for a single-phase flow. In Sec. III.B, an in-depth analysis of the particulate phase is conducted, including concentration statistics, spatial distribution, velocity and velocity fluctuations, as well as the particle accumulation near free surface. Additionally, an examination of the particle transport mechanism in the open square duct is presented. Finally, the concluding remarks are summarized in Sec. IV.

II. METHODOLOGY

A. Flow simulation

Figure 1 displays the geometry of the open square duct along with the coordinate system used in this study. The origin of the Cartesian coordinate system is at the centre of the duct, with the x-axis representing the streamwise direction and the y- and z-axes representing for the transverse and spanwise directions, respectively. The velocity components in the (x, y, z) directions are denoted as (u, v, w), and the dimensions of the domain are $8\pi h \times 2h \times 2h$. The streamwise length of the domain has been previously demonstrated to be sufficient to accommodate the longest streamwise-orientated near-wall turbulent structures in square duct flows [30-32]. The flow is assumed to be periodic in the streamwise direction, and no-slip conditions are imposed on the side and bottom walls of the duct. On the top free boundary, the condition of a rigid free-slip wall is applied:

$$\frac{\partial u}{\partial y} = \frac{\partial w}{\partial y} = v = 0 \tag{1}$$

The deformation of the free surface is not considered in the present study. Consequently, the abovementioned free-

slip boundary can be employed as an approximation for the flat surface [26]. The bulk Reynolds number, denoted as $Re_b = u_b h/\nu$, is set to be 5010 for the current flow, with a corresponding shear Reynolds number of $Re_\tau = 300$. Here, h is the half-width of the duct, ν is the kinematic viscosity of the fluid, and u_b is the bulk velocity. All quantities presented are normalized with respect to the integral scales of the bulk velocity u_b and length h, indicated by the superscript "*", or with respect to the viscous scales of the mean friction velocity $u_\tau = \sqrt{\bar{\tau}_w/\rho_f}$ and length $l_\tau = \nu/u_\tau$, denoted by the superscript "+". Here, $\bar{\tau}_w$ is mean shear stress exerted over the duct walls and ρ_f represents the density of the fluid.
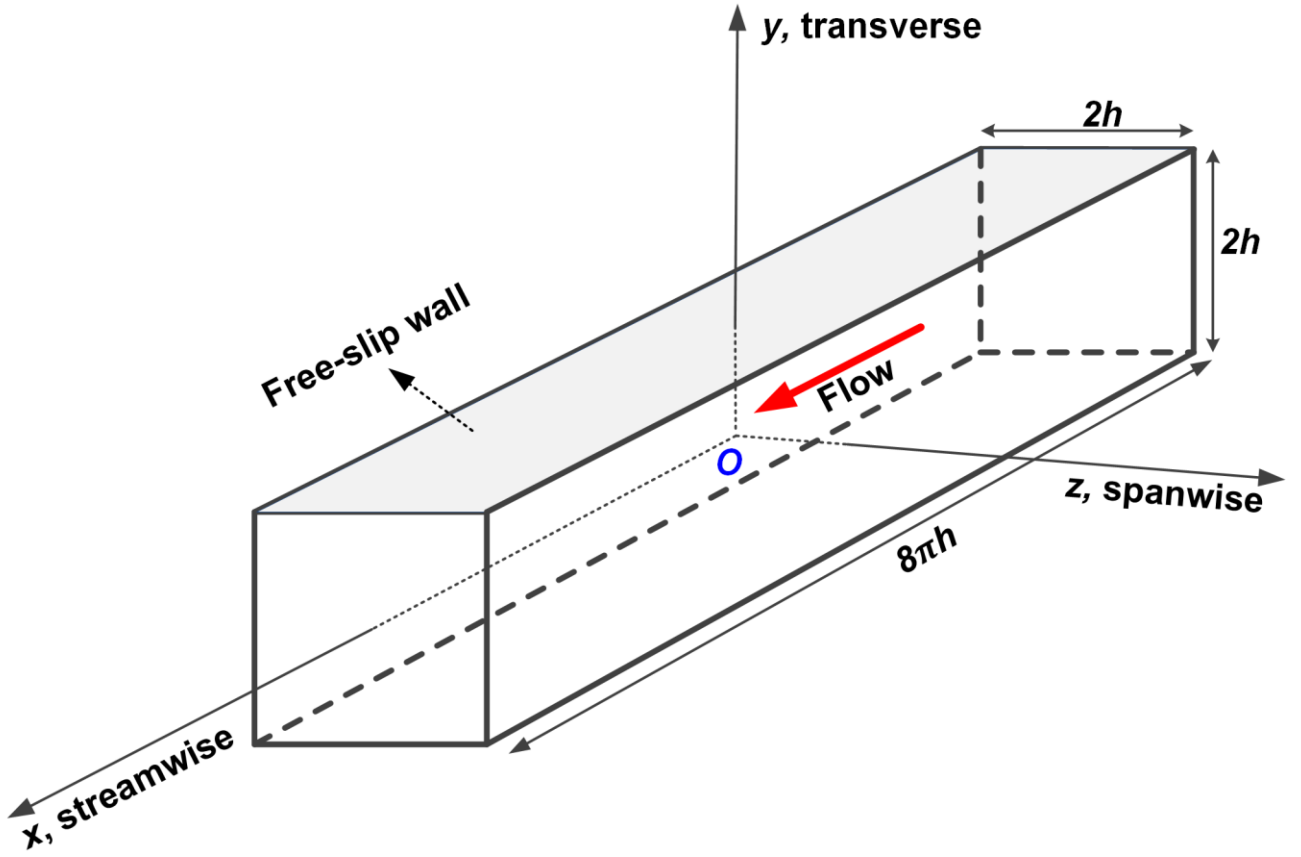

FIG. 1. Coordinate system and geometry of the computational domain.

The numerical solution for an incompressible Newtonian flow is obtained by using direct numerical simulation based on the spectral-element method, specifically using the Nek5000 code [33], which has been validated and extensively discussed in our previous study [17]. Here, only the essential details are provided. The Navier-Stokes equations, which are nondimensionalized based on the integral scales, can be expressed as follows:

$$\nabla \cdot \boldsymbol{u}^* = 0 \tag{2}$$

$$\frac{\partial \boldsymbol{u}^*}{\partial t^*} + \boldsymbol{u}^* \cdot \nabla \boldsymbol{u}^* = -\nabla p^* + \frac{1}{Re_b} \nabla \cdot \boldsymbol{\tau}^* + \boldsymbol{f}^* \tag{3}$$

where $\boldsymbol{u}^*$ represents the fluid velocity, p^* the fluid pressure and $\boldsymbol{\tau}^*$ the viscous stress tensor. To maintain a constant mass flow rate, a pressure gradient dynamically adjusted at every time step is employed in the streamwise direction, which is denoted as the additional source term $\boldsymbol{f}^*$ in Eq. (3). The computational domain is discretized using a nonuniform mesh consisting of $48 \times 24 \times 24$ elements. Within each element, the solution is represented at the GLL quadrature points of eighth-order Lagrange polynomials for the velocity, and two degrees lower Lagrange polynomials for the pressure. The spectral elements are uniformly distributed along the streamwise direction, with the corresponding grid point spacing ranging from $\Delta x^+ = 10.05 - 30.65$. In the wall-normal directions (y and z) the mesh nodes are clustered towards the wall or free surface, with the grid spacing ranging from $\Delta y^+ (\Delta z^+) = 0.38 - 12.30$. Throughout the simulation the average values for Δx^+ and $\Delta y^+ (\Delta z^+)$ are 22.36 and 3.55, respectively. Moving from the wall region towards the duct centre along the bottom-wall bisector, the ratio of the grid size to the local Kolmogorov length scale varies from $\Delta y / \eta_K$=0.11~3.67. The first grid point at the boundary is located at $y^+ = 0.41$, and 13 points are distributed in the near-wall viscous region of $y^+ < 10$. In this regard, grid spacings equal or smaller than η_K are considered too stringent because the Kolmogorov length scale is at the far end of the dissipative range[32]. Moreover, Vreman and Kuerten [34] has shown that most of the dissipation in a turbulent channel flow occurs at scales greater than $30\eta_K$. Therefore, the mesh used at the present Reynolds number is thought to be fine enough to resolve all relevant spatial turbulent scales. The same grid resolution was also used in our previous work on closed square duct flow at the similar Reynolds number [17], where the mean flow first- and second-order statistics obtained were found to be in good agreement with the previous DNS study of Vinuesa et al [35] using higher-order accuracy. Regarding the time-step, a small fixed dimensionless integration time step of $\Delta t^* = 0.002$, or equivalently $\Delta t^+ = 0.0368$, is used, ensuring that the CFL value remains smaller than 0.5 throughout the simulation. Further details about the numerical solution can be found in our previous study [17].

B. Particle motion

In the present particle-laden flow, the volume fraction ($\emptyset_V \leq 10^{-4}$) of particles is sufficiently low so that their effect on the fluid phase can be neglected. The particles are assumed to be small rigid spheres with identical diameter and density. Additionally, the particle size in magnitude is on the order of the Kolmogorov length scale η_K, which is based on the time-and space-averaged dissipation rate of the flow. According to the work of Bagchi and Balachandar [36], the turbulence effect on the drag and lift of a particle can be accurately predicted when the particle diameter is

within the range of $1.5\eta_\kappa < d_p < 10\eta_\kappa$. Therefore, the point-source method of a one-way coupled Lagrangian particle tracking technique is employed to simulate the transportation of particles in this work. The motion of the particles is governed by the drag, shear induced Saffman lift, virtual mass and pressure gradient force. Accordingly, the dimensionless equations of particle motion can be expressed as:

$$\frac{d\boldsymbol{u}_p^*}{dt^*} = \frac{3C_D|\boldsymbol{u}_s^*|}{4d_p^*\rho_p^*}\boldsymbol{u}_s^* + \frac{3C_L}{4\rho_p^*}(\boldsymbol{u}_s^* \times \boldsymbol{\omega}^*) + \frac{C_{am}}{\rho_p^*}\left(\frac{D\boldsymbol{u}^*}{Dt^*} - \frac{d\boldsymbol{u}_p^*}{dt^*}\right) + \frac{1}{\rho_p^*}\frac{D\boldsymbol{u}^*}{Dt^*} \tag{4}$$

$$\frac{d\boldsymbol{x}_p^*}{dt^*} = \boldsymbol{u}_p^* \tag{5}$$

where $\boldsymbol{x}_p^*$ represents the particle position, $\boldsymbol{u}_p^*$ is the particle velocity, $\boldsymbol{u}_s^*$ is the relative slip velocity between the two phases (with the fluid velocity at the particle location obtained through spectral interpolation), d_p^* is the particle diameter, and ρ_p^* is the ratio of particle to fluid density. C_D is the Stokes drag coefficient, C_L is the shear induced lift coefficient, the expressions for C_D and C_L, which also account for near-wall corrections, can be found in the literature [37]. The coefficient of the added-mass force, C_{am}, is set to 0.5. The terms $\boldsymbol{\omega}^*$ and $D\boldsymbol{u}^*/Dt^*$ is the fluid vorticity and fluid acceleration at the particle location, respectively. In addition to the forces mentioned in Eq. (4), particles are theoretically subjected to other forces such as electrostatic force[38,39], Basset history force, Magnus force, gravity, and buoyancy. However, in this study, the electrostatic force is disregarded due to the assumption that the particles and duct walls were electrostatically neutral. As for the Basset history force, previous studies[40-42] indicate that the contribution of this force is much smaller than that of the drag force when the particle size $d_p^+ \leq O(1)$. This force can therefore justifiably be neglected in the present work, with the additional benefit of significant savings of computational resources. Gravity and buoyancy are also not considered to isolate the impact of secondary flows on particle behaviour allowing detailed analysis of their influence. Similar assumptions were also made in the aforementioned works of Phares and Sharma [12] and Noorani et al [14] which considered closed duct flows. Furthermore, the remaining forces, which have been shown to be at least two orders of magnitude smaller than the forces considered in this study [42], are excluded from consideration.

During each time step, the equations of motion for each particle were integrated and solved using a Fourth-order Runge–Kutta scheme. The integration time step matched the flow time step and was chosen to be smaller than the minimum particle relaxation time to ensure that the particle trajectories were completely resolved. Particles were initially distributed randomly throughout the domain, and their initial velocity was set equal to the spectrally interpolated flow velocity at the particle position. Particle-wall collisions were treated as fully elastic, whereas the free-slip boundary was assumed to be completely absorbing. In other words, if the distance between a particle and

the upper free boundary was less than one particle diameter, the particle would be removed from the computational domain, and a new random particle would be introduced to maintain a constant number of particles. It should be mentioned that the number of particles leaving the free surface is very low, with the maximum average percentage of particles leaving the free-slip boundary per convection time unit relative to the total number of particles being 0.39% in the present simulation. In the streamwise direction, particles that moved out of the open square duct re-entered the domain by applying periodic boundary conditions.

TABLE I. Simulation parameters for the particulate phase.

Parameter		$St^+\approx0.31$	$St^+\approx25$	$St^+\approx125$	$St^+\approx260$
Number of particles	N_p			100,000	
Particle diameter	d_p^*			0.005	
	d_p^+			1.5	
Particle and fluid time step	Δt^*			0.002	
	Δt^+			0.0368	
Particle volume fraction	$\emptyset_V$			10^{-4}	
Bulk Stokes number	St_b	0.017	1.36	6.79	14.10
Shear Stokes number	St^+	0.31	25.0	125.0	259.5
Density ratio	ρ_p^*	2.5	200	1000	2076

Four particle populations with different particle-to-fluid density ratios (ρ_p^*=2.5~2076) are considered in this study. These ratios are chosen to simulate the physical scenarios where the continuous phase varies from water to air, while considering the particle material as glass. The physical particle diameter is fixed at d_p=100 μm, which corresponds to the dimensionless values of d_p^*=0.005 or d_p^+=1.5. The total number of particles used for each particle population is N_p=100,000, which is sufficiently large enough to ensure the independence of particle statistics on particle number. The particle relaxation time in viscous units (shear Stokes number) is defined as $St^+ = Re_\tau^2 d_p^{*2} \rho_p^*/18$, which ranges from St^+=0.31~260. In contrast, the corresponding particle relaxation time in outer units (bulk Stokes number) is given as $St_b = Re_b d_p^{*2} \rho_p^*/18$. The simulation parameters for the particulate phase are summarized in detail in Table I.

III. RESULTS AND DISCUSSION

A. Fluid phase

In the simulation of the fluid phase, the flow field was initialized using a fully developed channel flow at the

same Reynolds number. Then, the time history of the mean streamwise velocity, velocity fluctuations and wall shear stress along the bottom-wall bisectors was monitored until the flow reached a statistically steady state. Following this, data for the flow statistics were collected for an additional 1000 integral time units. Considering the streamwise homogeneity and geometric symmetry of the open square duct, the mean flow statistics discussed henceforth were obtained by simultaneously averaging in time, in the streamwise direction, and across the symmetry plane (the bottom-wall bisector).

Figure 2(a) presents the cross-sectional contours of mean streamwise flow velocity in half of the open square duct. The contour lines are clearly seen to bulge towards the lower corner and the juncture between the sidewall and free surface in the upper corner. Figure 2(b) further illustrates the contour of the magnitude of the mean secondary velocity ($\sqrt{V^{*2} + W^{*2}}$) along with its corresponding velocity vectors. Two counter-rotating secondary vortices are observed in the lower corner, responsible for transporting high-momentum fluid from the duct core region to the corner. As a result, the isolines of mean streamwise velocity become distorted. These phenomena are similar to those previous findings in closed duct flow [11-13]. However, a noticeable distinction in the open square duct flow is that the two counter-rotating secondary vortices are no longer symmetric about the lower corner bisector due to the influence of the top free surface. Henceforth, the secondary flow located below the lower corner bisector will be referred to as the bottom secondary flow [20]. In the upper corner of the mixed boundary, a small counter-clockwise vortex is clearly observed, and it can transfer momentum from the free surface towards the corner. This small vortex, known as the inner secondary flow vortex according to Grega et al. [18], is caused by the anisotropy of local turbulent shear stress. Moreover, a larger secondary vortex is identified outside the inner secondary vortex, as depicted in the region within the highlighted red dashed ellipse in Fig. 2(b). Grega et al. [18] referred to this larger secondary vortex as the outer secondary flow, which is responsible for the convection of low-momentum fluid from the sidewall towards the free surface. It consists of two rotational centres. Note that the maximum mean secondary flow velocity in the duct cross-section is achieved on the free surface, reaching a value of 4.3% of the mean streamwise velocity, which is significantly greater than observed in closed duct flows. This observation aligns with Nikitin's findings in turbulent open rectangular ducts [22]. In addition, the cross-sectional contour of turbulence kinetic energy (TKE) is given in Fig. 2(c). It is observed that the TKE near the top free surface is considerably smaller compared to the region close to the wall, and this disparity can be attributed to the absence of mean shear near the free surface, resulting in negligible turbulence production and dissipation rates due to the zero-velocity gradient there [5]. Furthermore, a peak in TKE is observed along the sidewall near the free surface (highlighted with a red dash circle in Fig. 2(c)). Note that the position of this peak is located where the inner secondary vortex and outer secondary vortex interact (see the

corresponding location in Fig. 2(b)), and low-streamwise-momentum fluid from the sidewall region can then be transported to the bulk flow region and the free surface by the convection of these secondary vortices, which further causes the contour lines of the mean streamwise velocity to bulge towards the inner region of the duct cross section (see the region within with red dash circle in Fig. 2(a)). Additionally, low-momentum fluid from the sidewall region has relatively high levels of turbulence, which thus leads to the higher streamwise fluctuations and TKE at this location. Overall, these findings are qualitatively consistent with the numerical results of Broglia et al. [5] in turbulent open square duct flows.
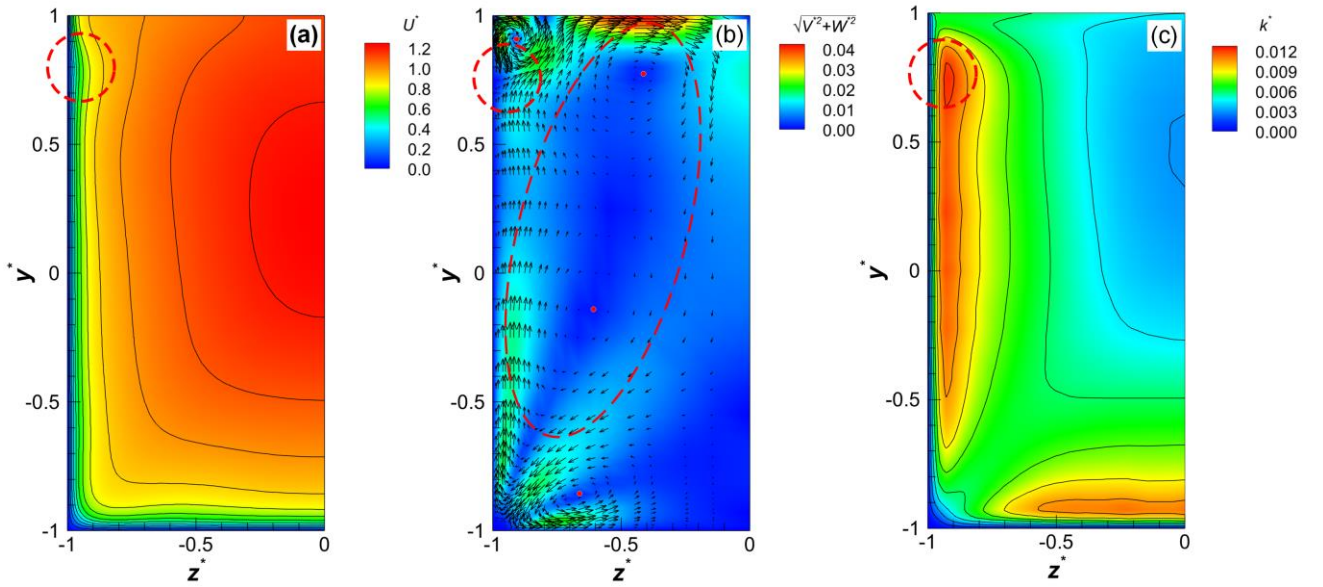

FIG. 2. Contours of the average flow statistics normalized by bulk velocity in half of the open square duct: (a) mean streamwise velocity, (b) magnitude of mean secondary flow velocity with its corresponding velocity vectors superimposed, and (c) turbulence kinetic energy.

In Fig. 3(a), the profile of the mean streamwise velocity in wall units along the bottom-wall bisector is compared to the large eddy simulation (LES) results of Broglia et al. [5]. A small discrepancy in the position of the maximum streamwise velocity between the two studies can be observed. This discrepancy is likely due to the lower grid resolution used in the LES work and the effect of the subgrid-scale model used, which may result in an underprediction of the intensities of the mean inner and outer secondary flows in the cross-sectional plane. Hence, the streamwise momentum in the present DNS is more affected by the convection of mean cross-sectional vortices, leading to a further displacement of the maximum mean streamwise velocity away from the free surface. Figure 3(b) shows a comparison of the mean streamwise-velocity based on the integral scale along the bottom-wall bisector

between open and closed duct flow [17] at a similar Reynolds number. In contrast to the closed duct flow, the maximum mean streamwise velocity is located at $y^*=0.22$ under the free surface in the open duct flow, which is attributable to the distinct distribution of the mean secondary flow along the bottom wall bisector in this duct. Considering this with Fig. 2(b), it can be further noted that the position of the maximum streamwise velocity in the transverse direction is close to the interface between the two vortices inside the mean outer secondary flow. Additionally, the mean streamwise velocity in the upper region of $y^* > 0.38$ is found to be larger than that in a closed duct flow, which is reasonable considering the reduced friction near a free surface compared to a solid wall. Profiles of the root mean square (r.m.s.) of velocity fluctuations compared with Broglia et al. [5] (in their work only the data near the free surface were provided) are presented in Fig. 3(c). The results indicate that the r.m.s. velocities in the surface-parallel directions (u^*_{rms} and w^*_{rms}) are significantly increased as the free surface is approached, whereas the r.m.s. velocity in the surface-normal direction is attenuated. As reported in Broglia et al. [5], this is related to the cross-sectional vorticial structures, which can transfer turbulence energy from the transverse components to the other two coordinate directions. Therefore, the TKE, dominated by the normal Reynolds stress (u^{*2}_{rms}), exhibits an increase near the free surface, confirming the observations in Fig. 2(c). Furthermore, it is noteworthy that the value of u^*_{rms} is smaller than that of w^*_{rms} at the free surface, which has also been previously observed by Shi et al. [43] in a rectangular open duct flow. This observation is significantly different from those recorded in relation to open channel flows, where the secondary flow is not relevant [27].

Figure 4 illustrates the distribution of the mean friction velocity normalized by its mean value along the sidewall in the present open square duct flow, compared to the results of Broglia et al. [5]. Consistent with the previous study, the mean friction velocity shows a trend of decreasing first then increasing as it approaches the free surface, with a minimum around $y^*=0.8$. This behaviour can be explained by the convection effect of the inner secondary vortex in the mixed boundary corner. The small difference in the minimum friction velocity between the present DNS and the LES of Broglia et al. [5] can be attributed to the varying accuracy in resolving the inner secondary flow. The above analysis confirms that the present DNS accurately captures the complex cross-flow turbulent vortices and generates an accurate flow field in the open square duct flow. Hence, it is expected that the influence of local turbulent flow structures on particle motion can be faithfully predicted in the two-phase flow simulations.
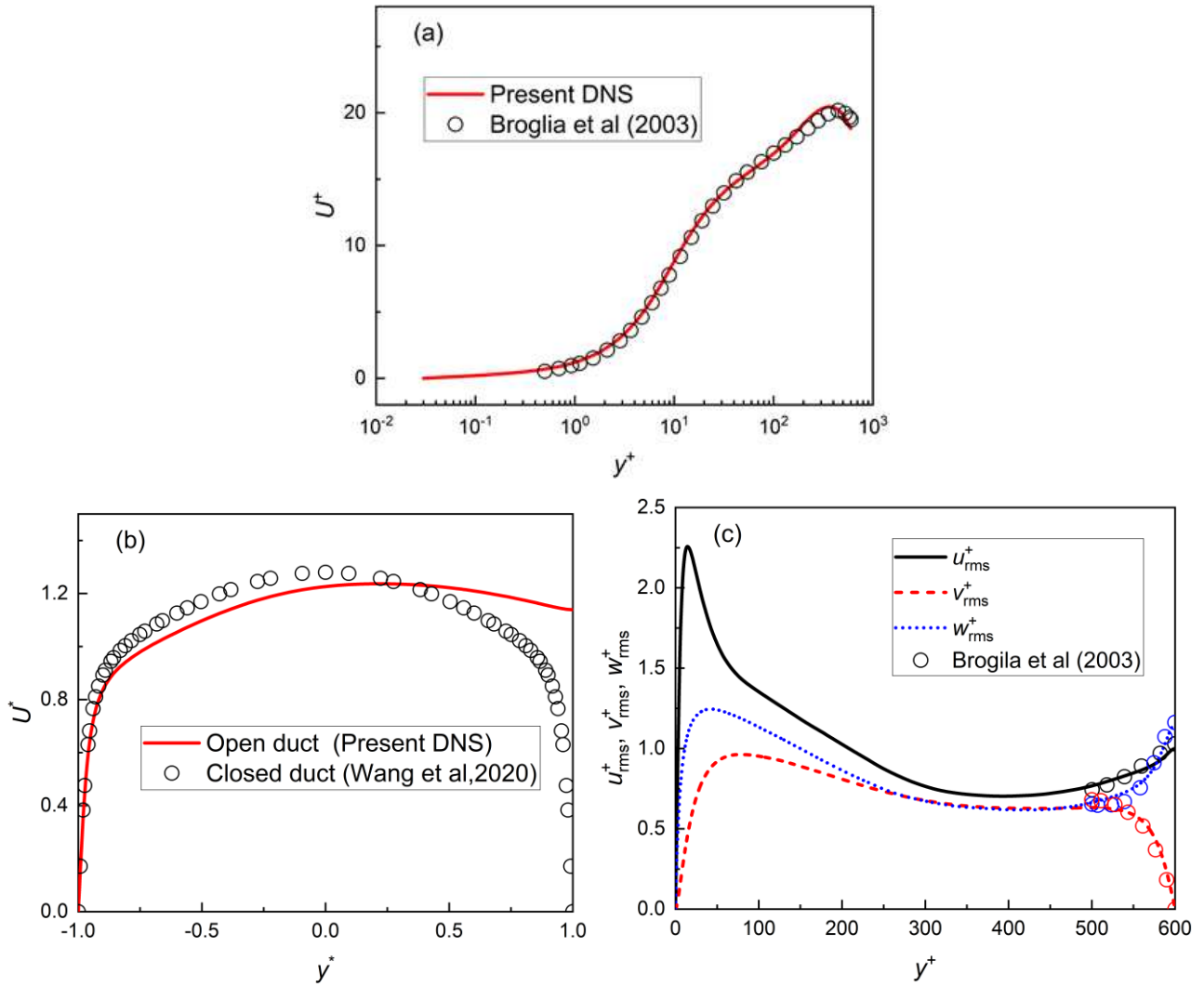
FIG. 3. Profiles of the average flow statistical moments along the bottom-wall bisector: mean streamwise velocity compared with (a) Broglia *et al.*[5] in open square duct and (b) Wang *et al.*[17] in closed square duct, (c) root mean square (rms) of velocity fluctuations.
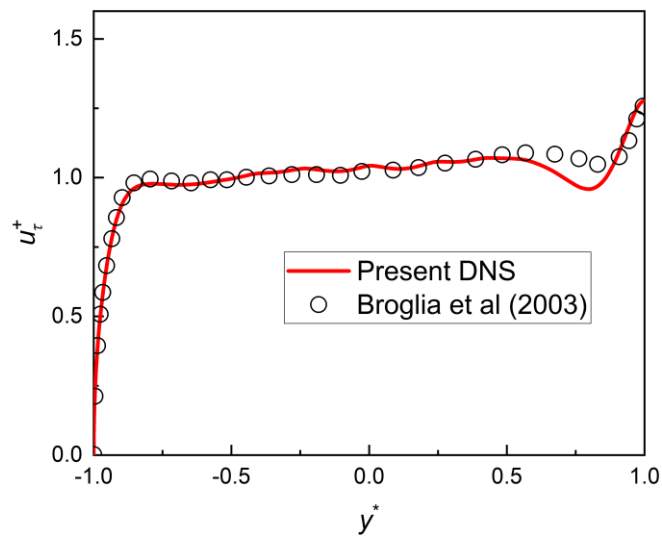

FIG. 4. Mean friction velocity distribution along the sidewall in comparison with Broglia *et al.*[5] in open square duct flow.

B. Particulate phase

Particles were released into the flow field once the fluid phase reached a fully developed turbulent state. The instantaneous particle concentration in the near wall region ($y^+ < 30$) was then monitored until particle dispersion in the entire domain reached a statistically steady state. Here, the particle concentration is defined as the number of particles per unit volume, normalized by the mean particle concentration in the whole open square duct. Figure 5 displays the temporal evolution of the instantaneous particle concentration C_w near the bottom wall and sidewalls. In Fig. 5(a), C_w of the heavier particles ($St^+ \geqslant 25$) first shows a rapid increase and then gradually stabilizes at around $t^* = 1000$ in the bottom wall region, where the particle accumulation behaviour is dominated by the mechanism of turbophoresis in canonical wall turbulence [44]. A similar trend is shared by the particle concentration in the sidewall regions as shown in Fig. 5(b), but C_w here is relatively smaller for the corresponding particles. This can be explained by the fact that the mean cross-sectional outer secondary flow entrains some particles away from the sidewall region. To visually present particle distribution in the duct cross section, a non-uniform two-dimensional grid [17] was used to calculate the Eulerian statistics of the particulate phase. Data was collected from time $t^* = 1000$, and averages over another period of 800 convection time units were conducted to obtain the presented mean particle statistics. The same spatial and temporal averaging method used for the fluid phase was also applied to the particulate phase.
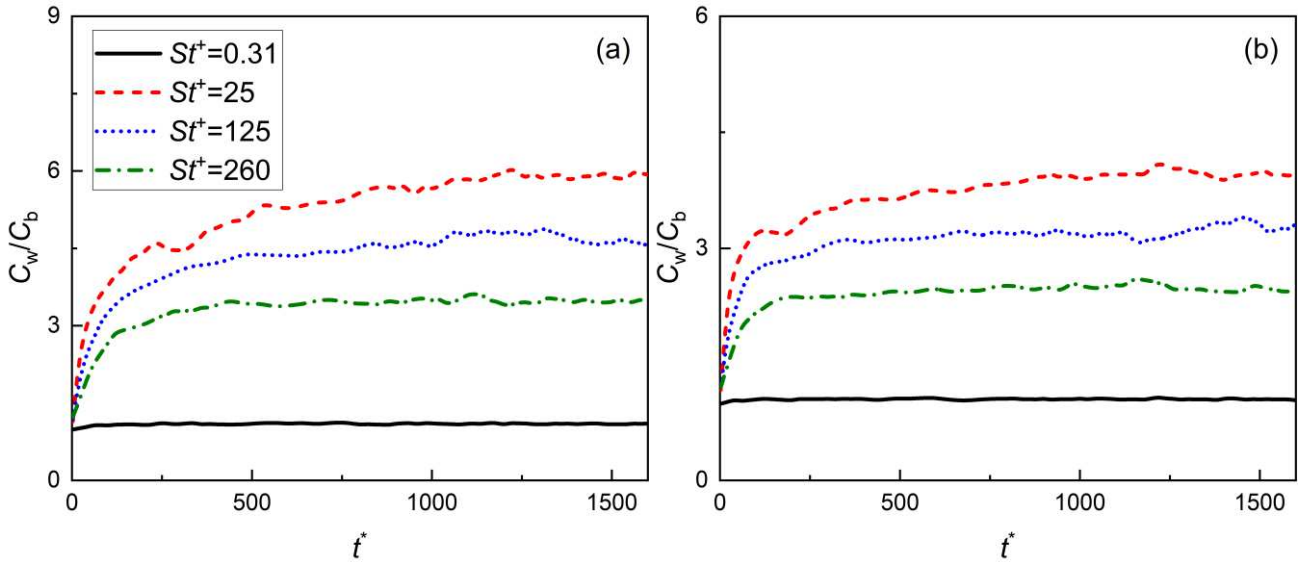

FIG. 5. Instantaneous particle concentration in the region of $y^+ < 30$ near the (a) bottom wall and (b) sidewalls normalized by the mean particle concentration in the whole domain versus dimensionless convective time for all particle Stokes numbers considered.

1. Particle concentration statistics

Figure 6 shows the contours of average normalized particle concentration on a logarithmic scale in the duct cross section for particles with $St^+=0.31\sim125$. It is evident that the lightest $St^+=0.31$ particles distribute uniformly over the cross-sectional plane due to their low inertia, while the heavier particles with $St^+\geqslant25$ accumulate in the near-wall region. Their concentration reaches a maximum in the lower corner of the duct, which is in line with previous findings in closed duct flow [17]. By contrast, the particle concentration near the free surface is significantly lower, suggesting that the effect of free-surface turbulence on particle distribution is distinctly different from near-wall turbulence in open square duct flow.
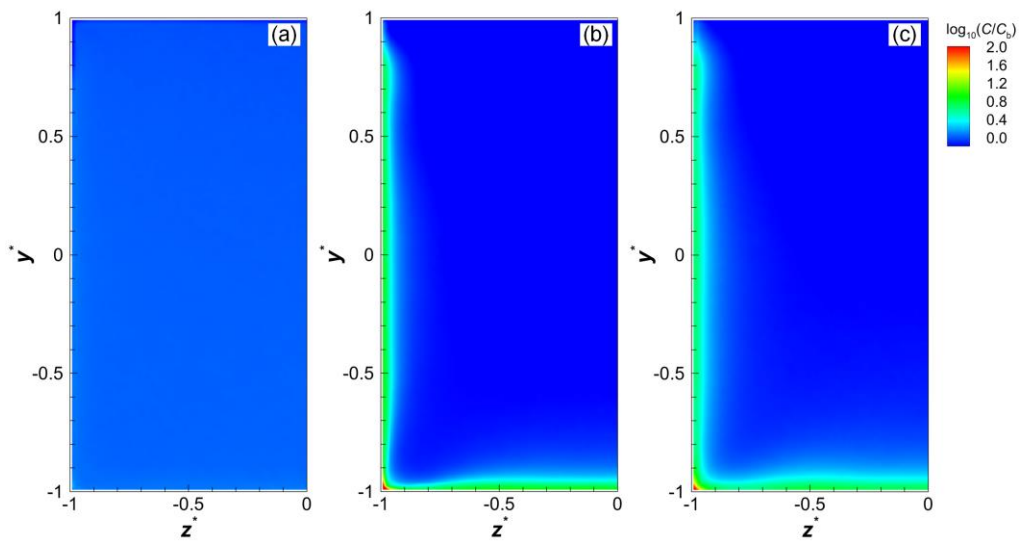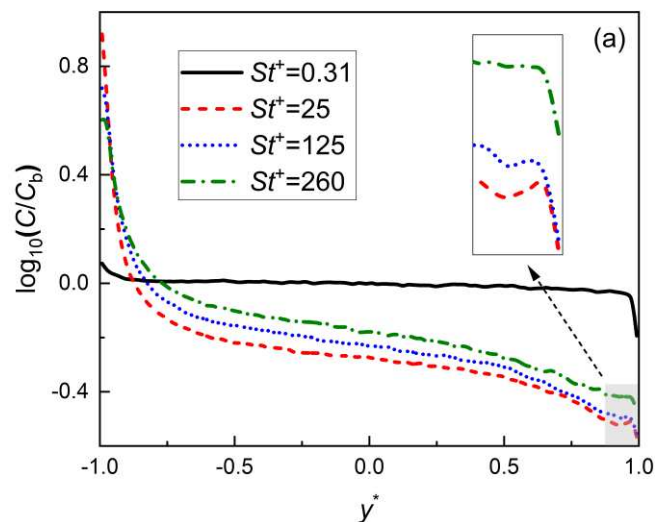

FIG. 6. Contours of the average normalized particle concentration (on a logarithmic scale) in the duct cross section for different particle Stokes numbers: (a)$St^+=0.31$, (b)$St^+=25$, and (c) $St^+=125$
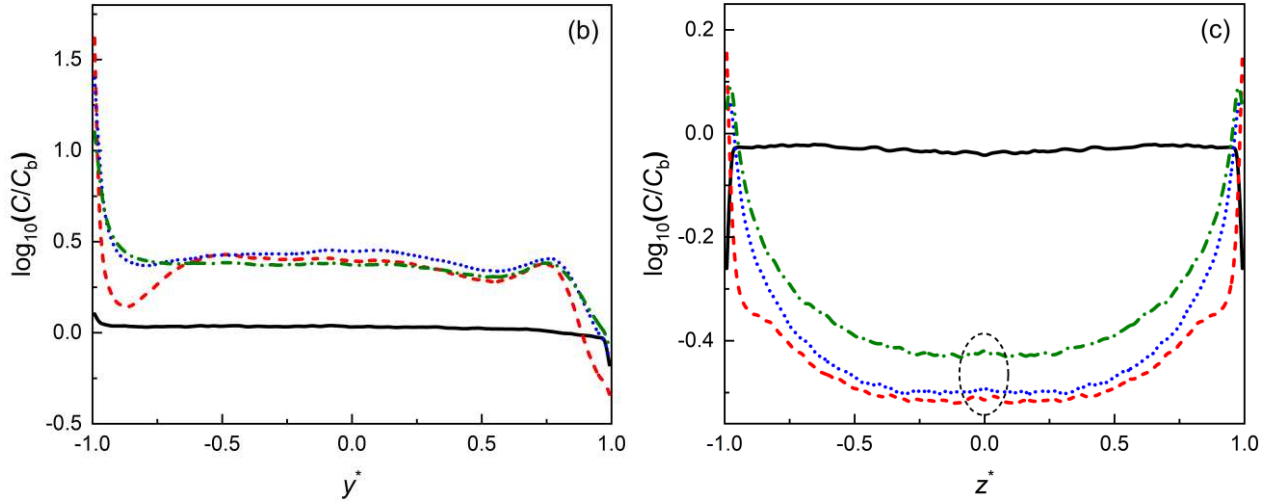
FIG. 7. Profiles of the average normalized particle concentration at (a) $z^* = 0$ along the bottom wall bisector, (b) at $z^* = -0.96$ near the sidewall, (c) at $y^* = 0.96$ along the free surface for all particle Stokes numbers considered.

To illustrate the effect of Stokes number on particle concentration, Fig. 7 presents the profiles of mean particle concentration along the bottom-wall bisector ($z^*=0$), the sidewall ($z^*=-0.96$) and free surface ($y^*=0.96$) extracted from Fig. 6 for the different particles. In Fig. 7(a), moving from the bottom to the free surface along the bottom-wall bisector, the magnitude of particle concentration gradually decreases for all particle sets. This declining trend is more pronounced closer to the wall. In the central region of the bottom wall ($y^* < -0.96$), which is one of the stagnation areas of the bottom secondary flow [14,17], the dependence of particle concentration on Stokes number is analogous to that in canonical channel flows [23,44], where the concentration maximum is observed for $St^+=25$ particles. Outside this region, the trend of particle concentration varying with Stokes number is exactly opposite due to the fixed total particle number in the entire domain. In particular, the concentration profiles for $St^+\geq25$ particles show a slight increase near the free surface, as seen in the local enlarged view of Fig. 7(a), and this increase becomes less significant with increasing particle Stokes number. This behaviour is consistent with previous observations in open channel flows and is primarily related to the effect of large-scale upwellings and downwellings of surface turbulence in these regions [26]. In the present open square duct flow, this behaviour is still affected by the downward mean secondary flow in this area.

Moving upwards along the sidewall from the lower duct corner, as depicted in Fig. 7(b), the concentration magnitude of particles with $St^+\geq25$ first decrease, reaching a minimum at approximately $y^*=-0.8$. Subsequently, it increases and stabilizes in the region of $-0.5 < y^* < 0.1$. This concentration minimum is caused by the transverse mean secondary flow, which possesses sufficient strength to displace most particles away from this region. The overall trend of particle concentration in the region $y^* < 0.1$ resembles that present in closed duct flows [17], despite the higher

intensity of the secondary flow in the current open square duct flow. As the upper corner is further approached, particle concentration slowly decreases until around y^*=0.55, and then gradually increases again before further declining at approximately y^*=0.75, with the minimum value occurring at the free surface. This trend can be explained by the combined effect of the inner secondary flow vortex and the outer secondary flow vortex in the mixed boundary region. On one hand, some particles in the vicinity of the sidewall can follow the upward movement of the outer secondary vortex, causing a decrease in particle concentration near the area of y^*=0.55. On the other, particles from the free surface tend to be transported towards the sidewall region at y^*=0.75 through the convection of the inner secondary vortex, resulting in particle accumulation in this area. Furthermore, it is noted that the extreme points of the concentration profile for St^+=25 particles are the most distinct, which is likely due to the fact that the nondimensional relaxation time of St^+=25 particles is closest to the characteristic time scale of the cross-sectional secondary vortices near the sidewall. As the Stokes number increases further, the distribution of particle concentration is less influenced by the cross-sectional secondary flow. Because of their lower inertia, St^+=0.31 particles located near the sidewall in the upper corner region can be entrained by the inner secondary flow to the lower part of the sidewall. Therefore, their concentration close to the upper sidewall region, as shown in Fig. 7(c), is relatively low, but it rapidly increases and becomes the highest along the free surface in the region of -0.8$\leq z^* \leq$0.8, whereas for particles with $St^+ \geq$25, their concentration gradually decreases along the free surface moving away from the sidewall. Furthermore, the slight increase in concentration for these particles in the central region of the free surface confirms the observations made in relation to the result of Fig. 7(a).

2. Particle spatial distribution

The Voronoi tessellation diagram, which has been widely employed for assessing particle distribution in wall-bounded turbulence [24,45], was utilized in this work to analyze the particle spatial distribution. The area of the Voronoi cells are inversely proportional to local instantaneous particle concentration. Accordingly, Fig. 8(a) gives the Voronoi diagram depicting a sample instantaneous realization for St^+=25 particles in the duct cross-sectional plane with particle cluster regions highlighted in blue. For clarity, only particles within the subzone of -5 $< x^* <$ 5 were used to generate the Voronoi diagram. It is clearly observed that particles tend to accumulate and form coherent clusters in the near-wall region, which can be explained by the effects of coherent ejections and sweeps present in near-wall turbulence. High-momentum fluid sweeps drive particles towards the wall, while low-momentum fluid ejections tend to push particles away from the wall. When the ejections lack sufficient strength to re-entrain particles into the outer bulk flow, particle accumulation near the wall occurs. This phenomenon agrees well with previous findings in

turbulent channel flows [46], and further details regarding the particle transport mechanism in near-wall turbulence can be found in Soldati and Marchioli [47]. It is also noted that some white regions can be observed in the top and middle plots of Fig. 8(b). No particles were found to be present in these regions, so the area of their corresponding Voronoi cells is infinitely large. For the present analysis of the particulate phase, these infinitely large Voronoi cells are invalid and thus have been removed from the plots. Furthermore, a distinctive mushroom-shaped outline of particle clusters is observed in the lower corner regions (see the highlighted areas marked in red in Fig. 8(a)). This pattern arises from the instantaneous cross-flow coherent structures associated with the generation of the mean secondary flows in the duct corner [48]. In contrast, particles are less concentrated near the free surface and upper corners of the duct. In addition to the secondary flow effects, the large-scale structures of shear-free surface turbulence may also play an important role. To provide further insight into the particle distribution in the flow direction, Fig. 8(b) presents the Voronoi diagrams overlaid with instantaneous particle distributions in the regions close to the free surface, sidewall, and bottom wall corresponding to Fig. 8(a) from top to bottom, respectively. Moreover, the Voronoi cells are colour-coded based on the streamwise velocity fluctuations at the particle locations. Particles are seen to accumulate in the low-velocity fluid streaks and form streamwise-elongated clusters near the sidewall and bottom wall regions, which is in agreement with the well-established phenomenon in wall-bounded turbulence [23,26,44]. However, the particle distribution near the free surface is observed to be disorganized, and there is no obvious correlation between particle accumulation and the streamwise velocity fluctuations. As shown in the upper plot in Fig. 8(b), $St^+=25$ particles near the free surface are not apparently concentrated in particular regions where the streamwise velocities are obviously higher or lower, as they are in the near wall region.
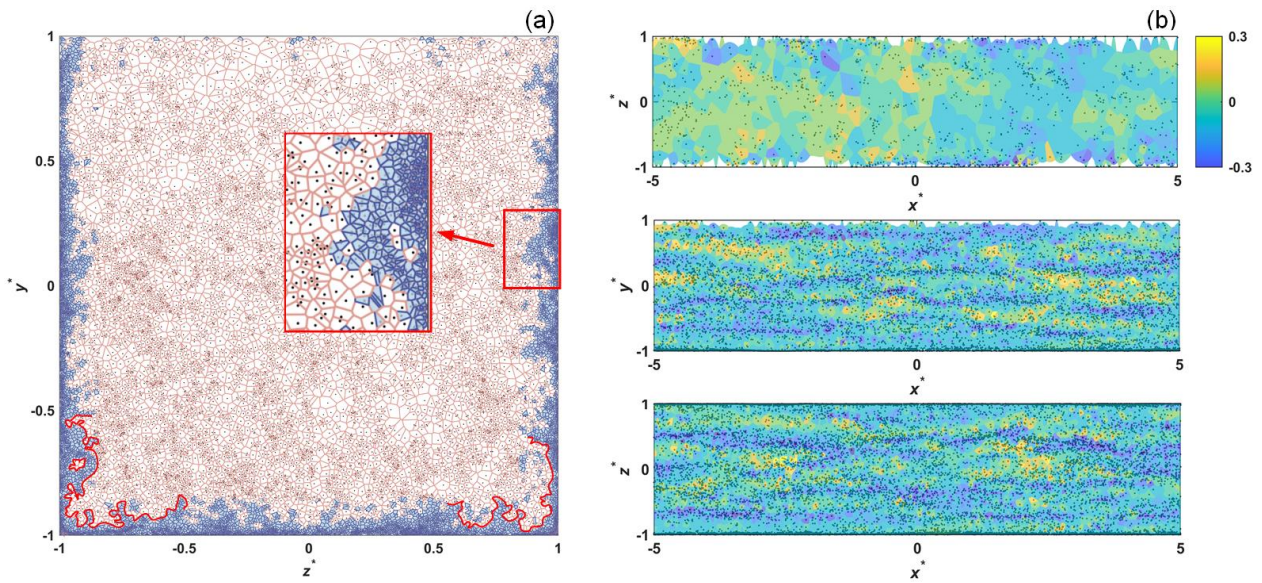

FIG. 8. Voronoi tessellation diagram for $St^+=25$ particles: (a) in the cross-sectional plane ($-5<x^*<5$) with cluster

regions highlighted in blue, and (b) in the regions close to the free surface (top), sidewall (middle), and bottom wall (bottom) ($y^+<30$) with the Voronoi cell coloured by the streamwise velocity fluctuations at the particle locations.
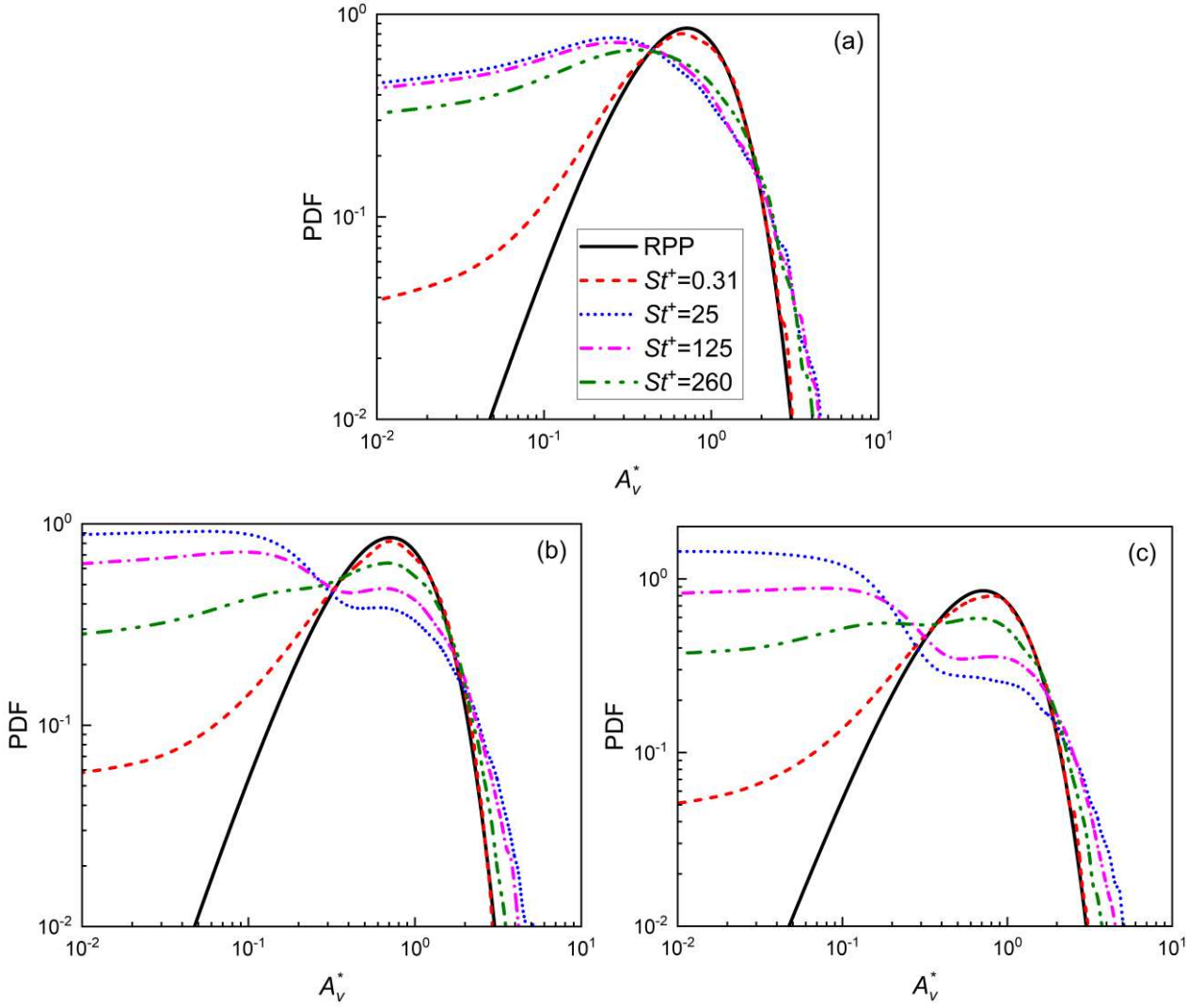

FIG. 9. PDFs of the Voronoi cell area compared with a random Poisson distribution for different particles in the region close to the (a) free surface, (b) sidewall and (c) bottom wall ($y^+<30$).

Regarding the effects of Stokes number, Fig. 9 plots the probability density functions (PDFs) of the Voronoi cell area A_v^* compared to a random Poisson distribution (RPP) for $St^+=0.31$ to 260 particles in the region close to the free surface, sidewall and bottom wall at the end of the simulation. The PDF values of all the particles for very small cell areas are found to be larger than those of the RPP in all three regions, suggesting that all the particles exhibit some degree of clustering, albeit at different levels of accumulation. By comparing the PDF values of small Voronoi cell areas for different particles, it can be concluded that the level of particle clustering initially increases then decreases with an increase in Stoke number, with the maximum clustering observed for $St^+=25$ particles. Furthermore, it should be noted that the PDF curves for the particles in the near-wall region of the sidewall and bottom wall exhibit similar

patterns, which indicates that the instantaneous distribution of most particles in the two regions is analogous. Combined with the results of Fig. 8 and Fig. 10, with the latter showing the PDFs of the instantaneous particle distribution along the wall-normal direction corresponding to Fig. 9, it can be inferred that particles with $St^+ \geq 25$ are the most clustered and tend to form thin particle streaks along the borderline in the lower corners, with the clustering level declining with Stokes number. Conversely, in the middle area of the bottom wall region, particles are prone to form streamwise-aligned streaky structures in low-speed fluid regions, as depicted in Fig. 8(b), with these regions corresponding to the peaks in the profiles of the PDFs shown in the local enlarged view of Figs. 10(b) and (c). Additionally, it is worth noting that the maximum values of the PDF peaks decreases with increasing Stoke number, indicating that because the heavier particles are more inertial, their motion is governed less by the local coherent turbulence structures and hence they are less likely to form elongated particle streaks in the wall-middle region. These observations are in agreement with previous findings in closed duct flows [17], where the fundamental mechanism for particle preferential concentration induced by turbulence-driven secondary flow was elucidated. Although the overall particle concentration near the free surface is much lower compared to the near-wall region, particles still exhibit some degree of preferential concentration, as observed in Figs. 9(a) and 10(a). Along the free surface near the upper corners, particles with $St^+ \geq 25$ are seen to have a higher concentration, which is due to the combined effects of coherent structures emanating from the sidewall and inner secondary flow in these areas. While in the middle region of the free surface, where particle motion is dominated by the free-surface turbulence vortices, particle accumulation is significantly attenuated, and its dependence on Stokes number is also weakened. Additionally, the strong spanwise secondary flow also plays an important role in the particle distribution near the free surface. The underlying mechanisms responsible for these distributions will be discussed later.
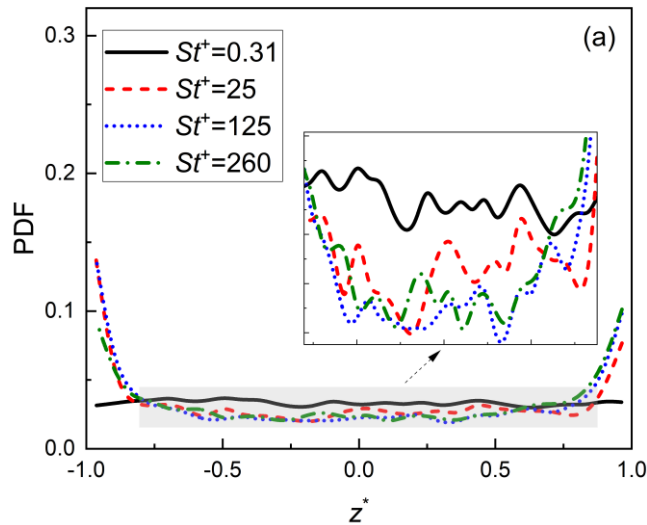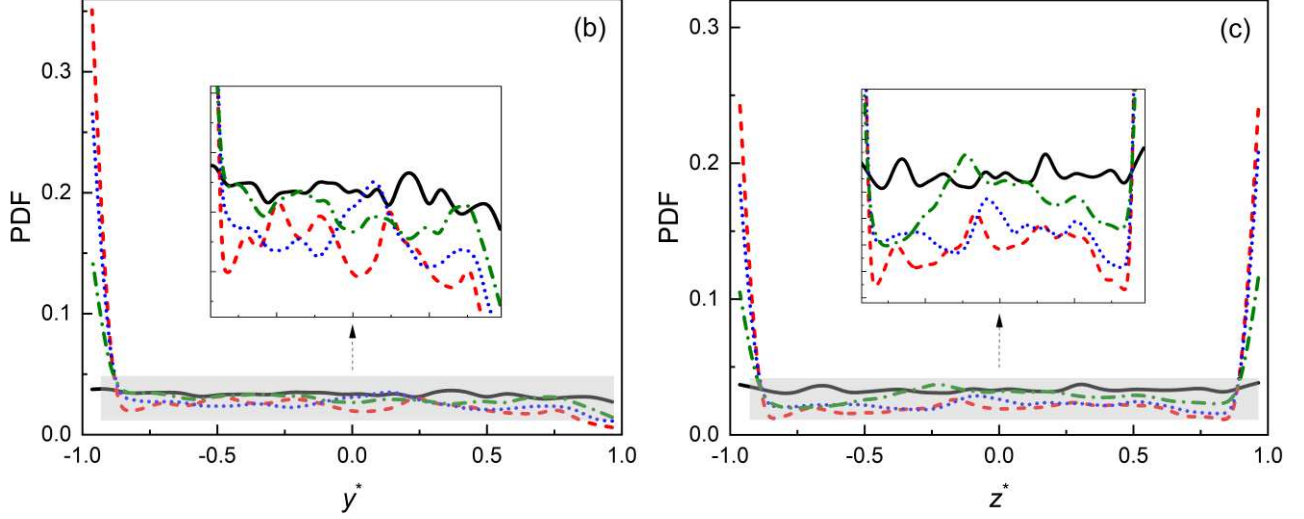
FIG. 10. PDFs of the instantaneous particle distribution along the wall-normal direction in the region close to the (a) free surface, (b) sidewall and (c) bottom wall corresponding to Fig. 9.

3. Particle velocities

To analyze the particle transport in the duct cross-section, Fig. 11 displays the contours of the mean streamwise particle velocity with their corresponding profiles along the bottom-wall bisector based on the integral scale and the viscous scale shown in Figs. 12(a) and 12(b), respectively. Generally, the contours of the mean streamwise particle velocity resemble that of the fluid phase in Fig. 2(a). Specifically, the profile of mean streamwise velocity for St^+=0.31 particles along the bottom-wall bisector coincides well with the fluid phase due to their low inertia, although a slight deviation is observed in the part of the buffer layer near the bottom wall. As the Stokes number increases, the streamwise particle velocity in the central region of the duct cross section (-0.5 < y^* < 0.5) gradually decreases. However, in the buffer layer of $5 < y^+ < 30$ shown in Fig. 12(b), an opposite trend is observed for particles with $St^+ \geq 25$. Like the turbulent particle-laden channel and closed square duct flows [17,44], this can be attributed to the fact that the heavier particles tend to accumulate in the low-streamwise-velocity regions as seen in Fig. 8, with this trend weakened with increasing Stokes number. For $St^+ \geq 25$ particles, it is noted that the mean streamwise velocity slightly increases with Stokes number along the bottom-wall bisector in the region of $y^* > 0.75$ near the free surface, as depicted in the local enlarged view of Fig. 12(a). Furthermore, the position of the mean maximum streamwise velocity, marked with solid triangle symbols in Fig. 12(a), is found to be closer to the free surface for the particles with higher inertia. These two phenomena are correlated and can be attributed to the different distribution of secondary particle velocities in the duct cross section, which will be further elaborated upon.
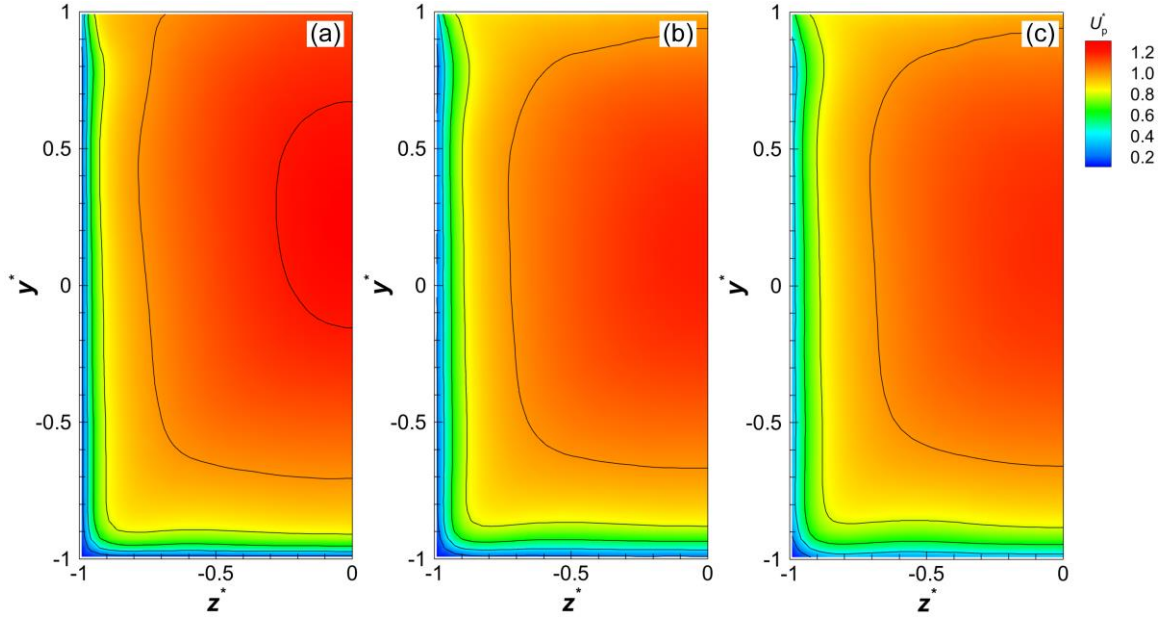
FIG. 11. Contours of mean streamwise particle velocity in the duct cross-section for particle with (a) St^+=0.31, (b) St^+=25, and (c) St^+=125.
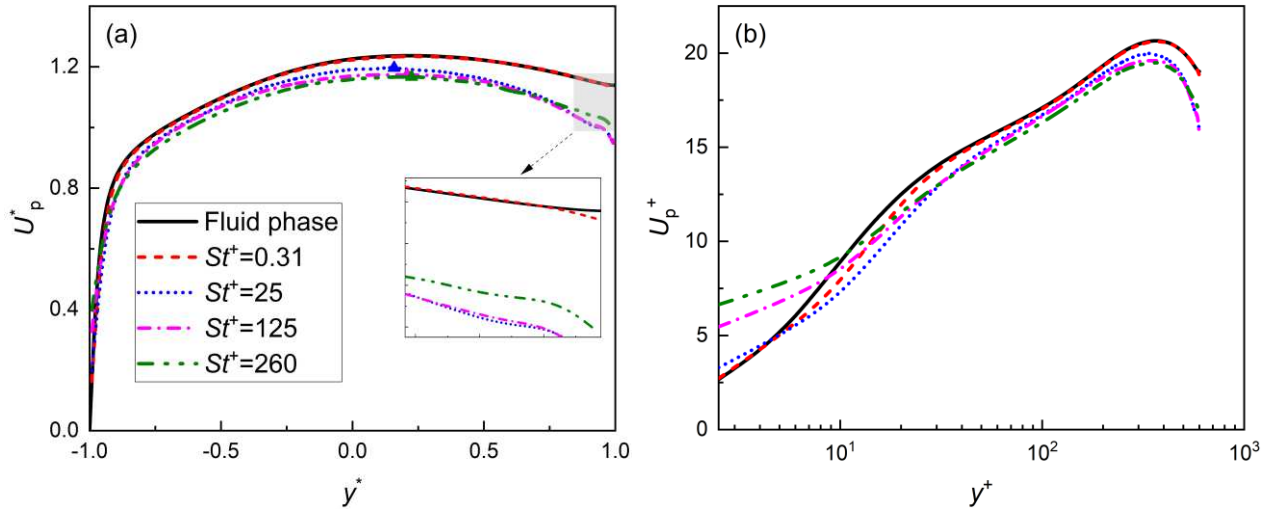

FIG. 12. Profiles of mean streamwise particle and fluid velocity along the bottom-wall bisector based on (a) the integral scale and (b) the viscous scale for the indicated particles.

Contours of the time and spatially-averaged secondary velocity magnitude ($\sqrt{V_p^{*2} + W_p^{*2}}$) superimposed with its corresponding vector fields for particles with St^+=0.31 to 125 are presented in Fig. 13. The distribution of the secondary motion velocity for St^+=0.31 particles is similar to that of the fluid phase in Fig. 2(b), implying that these particles closely follow the mean cross-sectional secondary flow vortices. With the increase in Stokes number, the location of the maximum secondary particle velocity changes, and the rotation centres of the inner and outer secondary particle motions gradually disappear. This is because the heavier particles have a longer relaxation time

and are unable to respond rapidly to the secondary flow motions in the upper half of the duct cross section. In the region below the lower corner bisector, which is also the area of the bottom secondary flow, the Stokes number dependence of particle secondary motions is found to be analogous to that in a closed square duct flow [17].
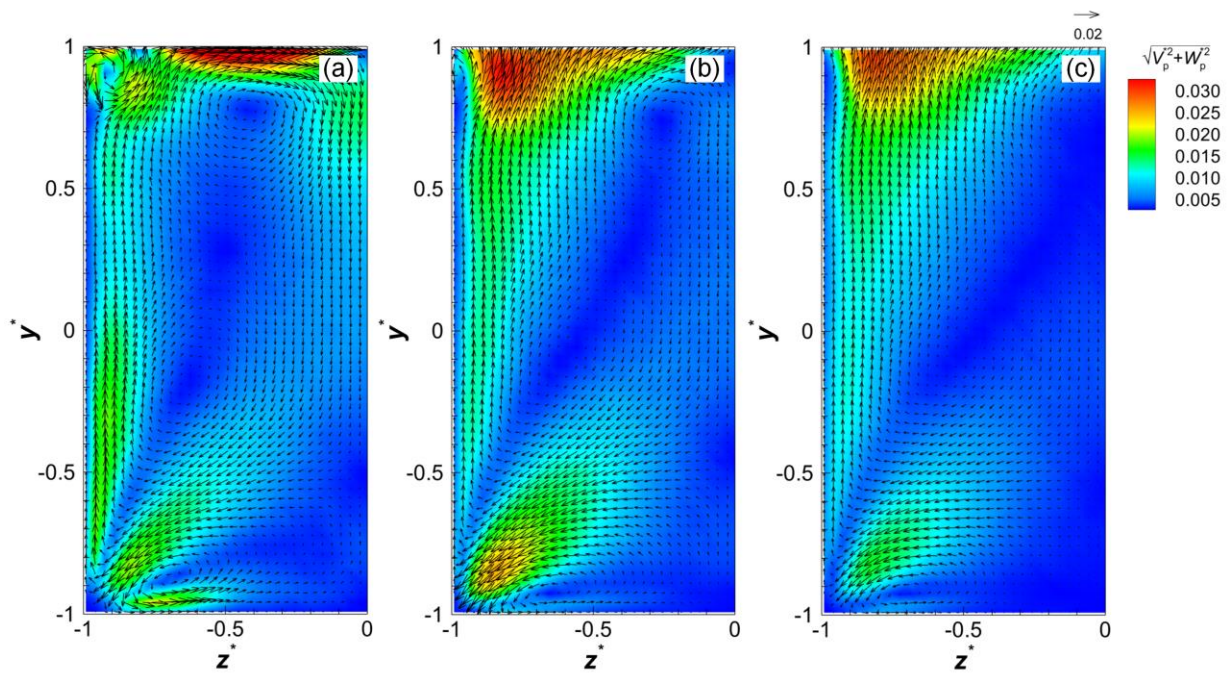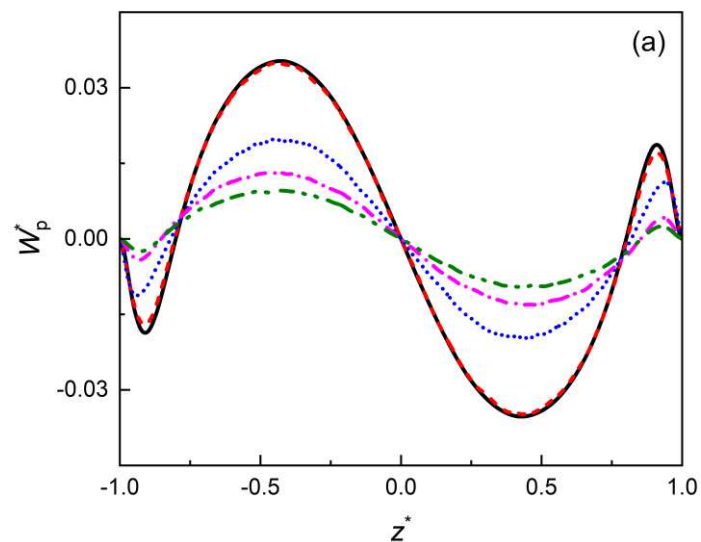

FIG. 13. Contours of time and spatially-averaged secondary motion velocity magnitude superimposed with its corresponding vector fields for particles with (a) St^+=0.31, (b) St^+=25, and (c) St^+=125.
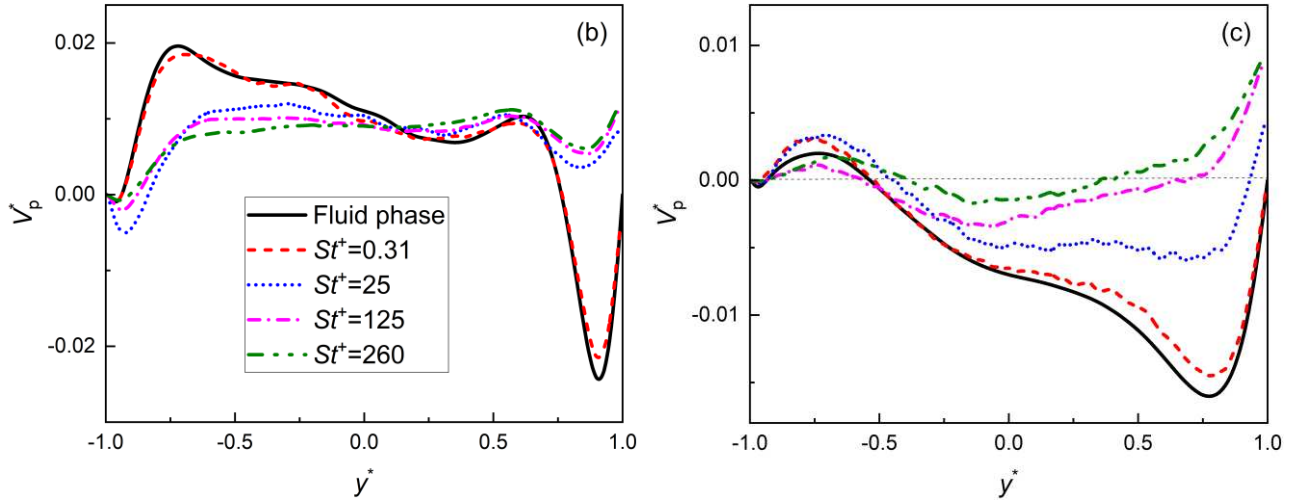
FIG. 14. Profiles of mean secondary particle and fluid velocity (a) in the spanwise direction at $y^* = 0.96$ along the free surface, (b) in the transverse direction at $z^* = -0.96$ along the sidewall, and (c) at $z^* = 0$ along the bottom wall bisector for all particle Stokes numbers considered.

In Fig. 14(a), the profiles of spanwise secondary particle velocity at $y^* = 0.96$ along the free surface for all investigated particles are displayed. As the particle inertia increases, the spanwise secondary particle velocity along the free surface is found to decrease in absolute value. The transverse components of secondary particle and fluid velocity at $z^* = -0.96$ along the sidewall and at $z^* = 0$ along the bottom wall bisector are presented in Figs. 14(b) and 14(c), respectively. In the region of $y^* > -0.5$, where the cross-sectional particle motions are dominated by the inner and outer secondary flows, the absolute transverse secondary particle velocity shows a similar dependence on the Stokes number as the spanwise component along the free surface. This indicates that the ability of particles to follow the inner and outer secondary flow decreases with increasing particle inertia. Whereas in the bottom area of $y^* < -0.5$, the transverse secondary velocity for $St^+ = 25$ particles is largely enhanced compared to that of the fluid phase, suggesting that the relaxion time for $St^+ = 25$ particles is closest to the characteristic time scale of the bottom secondary flow. This phenomenon is also observed in closed duct flows for the particles with the same Stokes number [17]. Furthermore, it is noted that the transverse secondary velocity of the $St^+ \geqslant 25$ particles shows a change in direction in the region of $y^* > -0.5$ along the bottom-wall bisector. Combined with the observations made in relation to Fig. 13, it can be inferred that more particles move upward along the bottom-wall bisector with increasing Stokes number. This upward movement of particles carries more momentum to the free surface, resulting in higher streamwise velocities for the heavier particles.

4. Particle velocity fluctuations

Figure 15 provides the contours of the TKE (k_p^*) for particles with St^+=0.31 to 125. It is observed that the local maxima of TKE for St^+≤25 particles occur in the buffer layer near the wall, which is due to the fact that these particles can quickly respond to the coherent structures with fast turbulent fluctuations in these regions. Conversely, the location of TKE maximum for particles with St^+= 125 are found to be closer to the wall. This can be understood by the high mean gradient of the streamwise velocity in the viscous sublayer, which can generate significant fluctuations in the particle streamwise velocity. This effect is more pronounced for particles with large Stokes numbers [49,50], despite the notion that higher inertia particles can filter out some of the fast turbulent motions in the near-wall region. Furthermore, note that there is a local minimum of TKE for all particles in the duct lower corner. Along the free surface, the particle TKE is relatively low, while the TKE in the upper corner increases with increasing Stokes number.
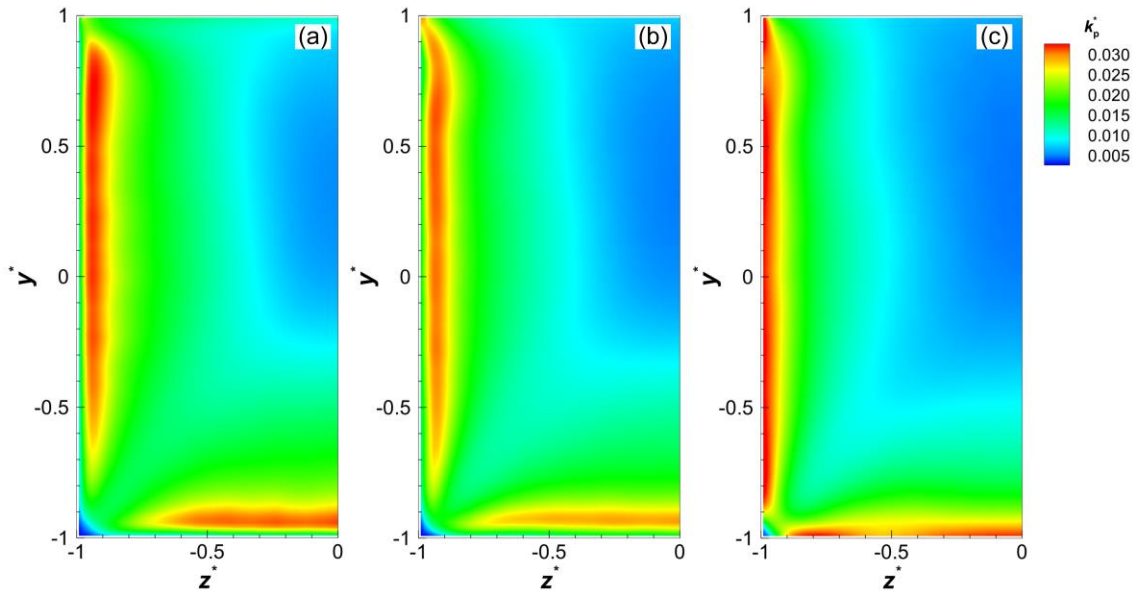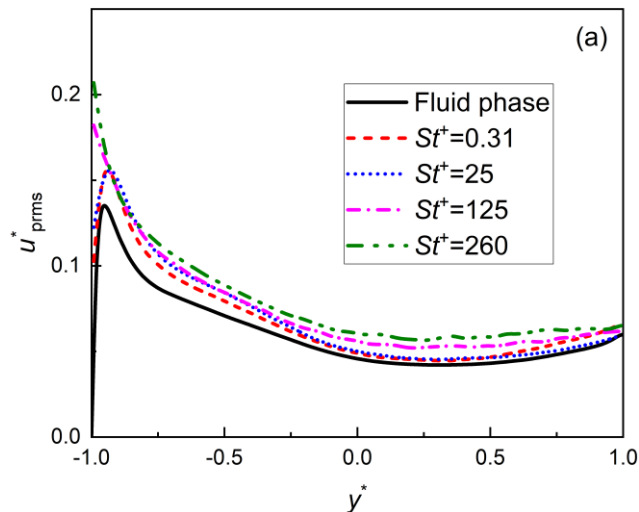

FIG. 15. Contours of the turbulence kinetic energy for particles with (a) St^+=0.31, (b) St^+=25, and (c) St^+=125.
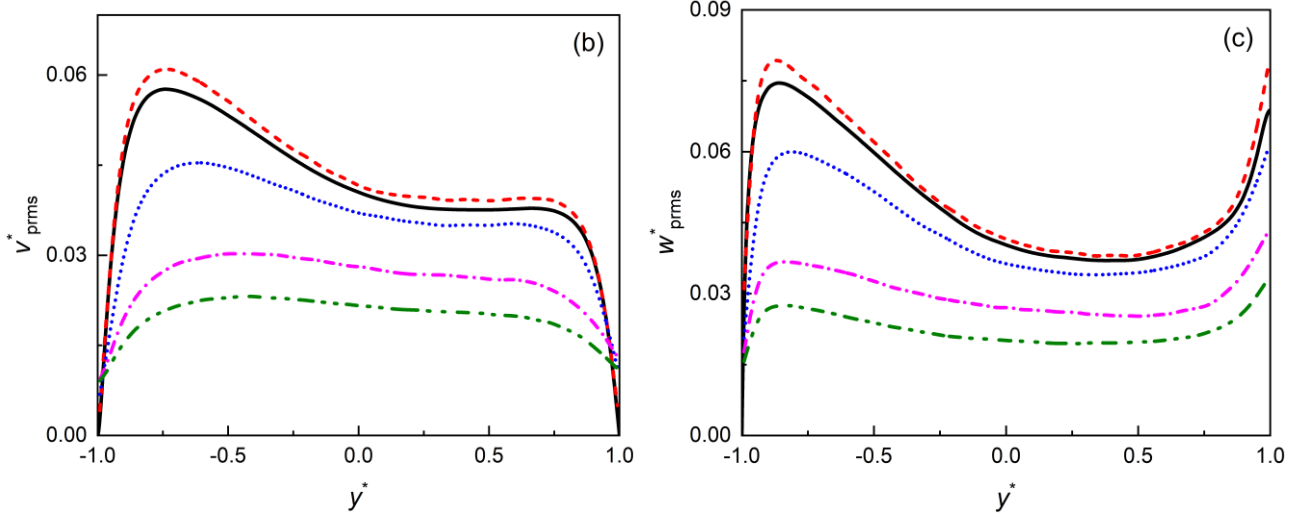
FIG. 16. Profiles of fluid and particle *r.m.s.* velocities along the bottom-wall bisector: (a) streamwise, (b) transverse and (c) spanwise component.

The profiles of *r.m.s.* velocities for both the fluid and particle phases along the bottom-wall bisector and along the free surface are shown in Figs. 16 and 17, respectively. As expected, the *r.m.s.* velocities in the streamwise direction for all inertial particles are larger than those of the fluid phase, as seen in Figs. 16(a) and 17(a). Moreover, the discrepancy between the two phases becomes more obvious as the particle Stokes number increases. This was previously explained by Portela *et al.* [50] who noted inertial particles can move between the regions of high and low streamwise velocity in the transverse direction due to their interaction with the local turbulence structures, considering the gradient of mean flow streamwise velocity. Nevertheless, it is worth noting from Fig. 17(a) that the streamwise *r.m.s.* velocity for the lightest $St^+=0.31$ particles is even larger than that of the higher-inertia particles in the central region ($-0.3 < z^* < 0.3$) of the free surface. This is possibly because $St^+=0.31$ particles can easily follow the outer secondary flow in this area and tend to distribute uniformly over the free surface. On the other hand, the heavier particles have a tendency to accumulate in the downwelling regions of turbulent flow structures, where the fluid streamwise *r.m.s.* velocity is relatively low. It should be mentioned that this phenomenon is also evident near the sidewall area, where the transverse outer secondary flow plays a crucial role. Similarly, the *r.m.s.* velocities of the $St^+=0.31$ particles in the transverse and spanwise directions along the bottom-wall bisector are observed to be enhanced compared to the fluid phase in Figs. 16(b) and 16(c), with this phenomenon more obvious along the free surface as shown in Fig. 17(c). This can be attributed to the nonzero gradient of the mean secondary flow velocity, which is absent in canonical turbulent channel flows. Near the free surface, the gradient direction of the secondary flow velocity is opposite to that near the wall. As a result, the low inertia particles can be easily entrained into the regions of higher secondary flow velocity, where the corresponding transverse or spanwise *r.m.s.* velocities are

relatively high. Conversely, the transverse and spanwise *r.m.s.* velocities for $St^+ \geq 25$ particles are largely suppressed as a result of inertial filtering, which is consistent with the results obtained in channel flows [26]. In particular, the transverse *r.m.s.* velocity for $St^+=25$ particles is also enhanced in the region of $-0.85<z^*<0.85$ along the free surface in Fig. 17(b). This is possibly associated with the strengthened transverse secondary particle velocity in this area, with the highest gradient of mean transverse secondary particle velocity found for the $St^+=25$ particles. The enhanced upward secondary particle velocity encourages more particles to move to the upwelling regions of fluid motion near the free surface, where the streamwise and transverse *r.m.s.* velocities are relatively high.
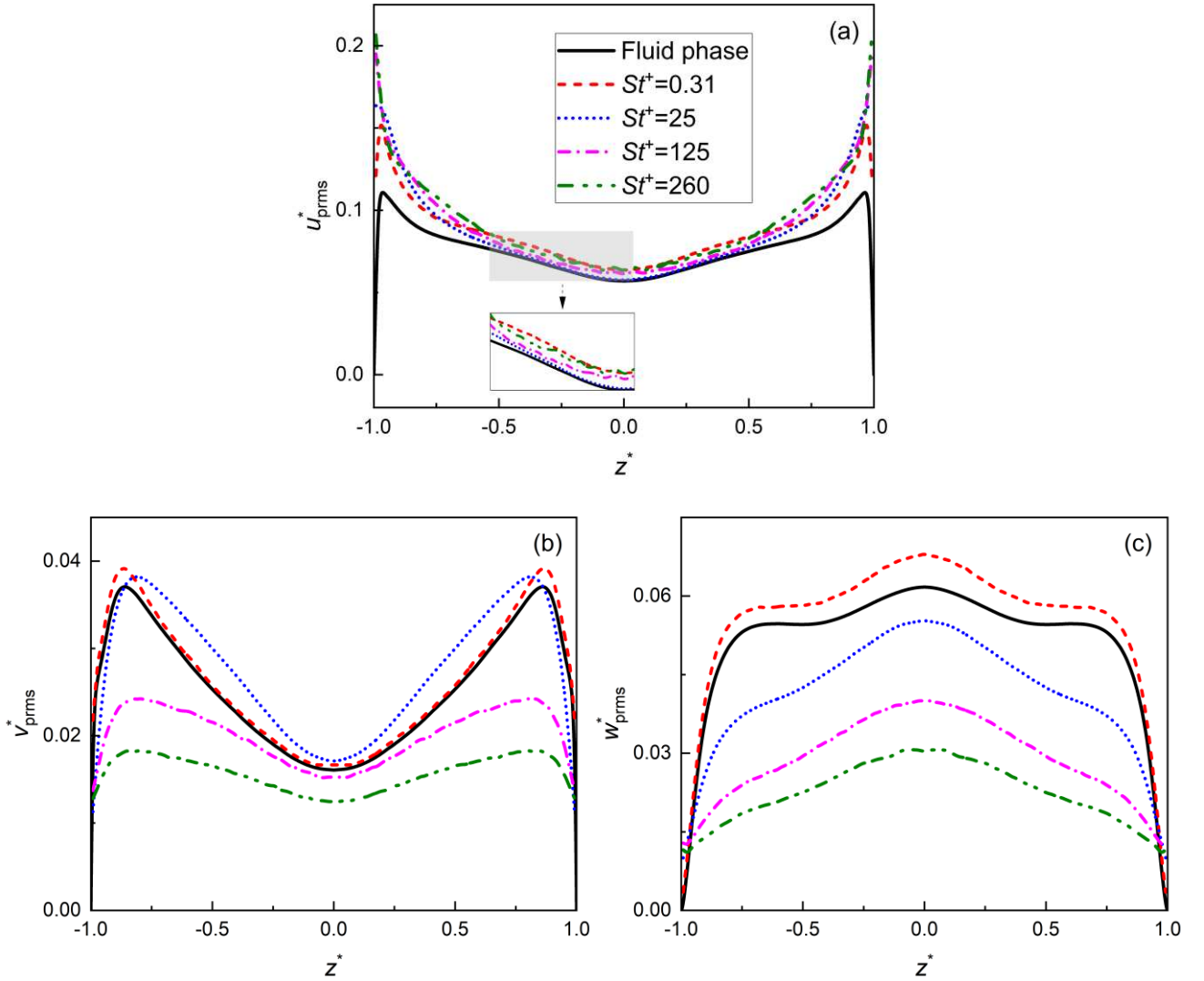

FIG. 17. Profiles of fluid and particle *r.m.s.* velocities near the free surface ($y^*=0.96$): (a) streamwise, (b) transverse and (c) spanwise component.

5. Particle accumulation near the free surface

A previous study [26] indicated that particle distributions near the free-slip surface are subjected to large-scale subsurface structures such as upwelling and downwelling motions of the fluid. Lovecchio et al [27,51] further discovered that light particles tend to cluster into filaments in the regions of downwelling near the free surface, where the turbulence is considered to be nearly two-dimensional. The surface divergence, defined as $\nabla_{2D} = \partial u / \partial x + \partial w / \partial z$, was used to distinguish between the areas of upwelling and downwelling. However, in the present open square duct flow, the existence of three-dimensional secondary flow in the cross section makes ∇_{2D} less accurate. Therefore, the instantaneous transverse fluid velocity v_f is directly adopted to differentiate between the areas of upwellings ($v_f < 0$) from downwellings ($v_f < 0$) in the present work. Figure 18 shows the instantaneous particle distributions superimposed with the contours of instantaneous transverse fluid velocity v_f at the particle locations near the free surface ($y^* > 0.9$) at the end of the simulation for all particle Stokes numbers considered. The regions marked in purple denote $v_f < 0$ (downwelling) while the regions marked in pink represent $v_f > 0$ (upwelling). It is observed that heavier particles with $St^+ \geq 25$ tend to cluster into inclined elongated particle streaks following the regions of $v_f < 0$, with the degree of particle accumulation attenuated with increasing Stokes number, which confirms the results of Fig. 8(a).
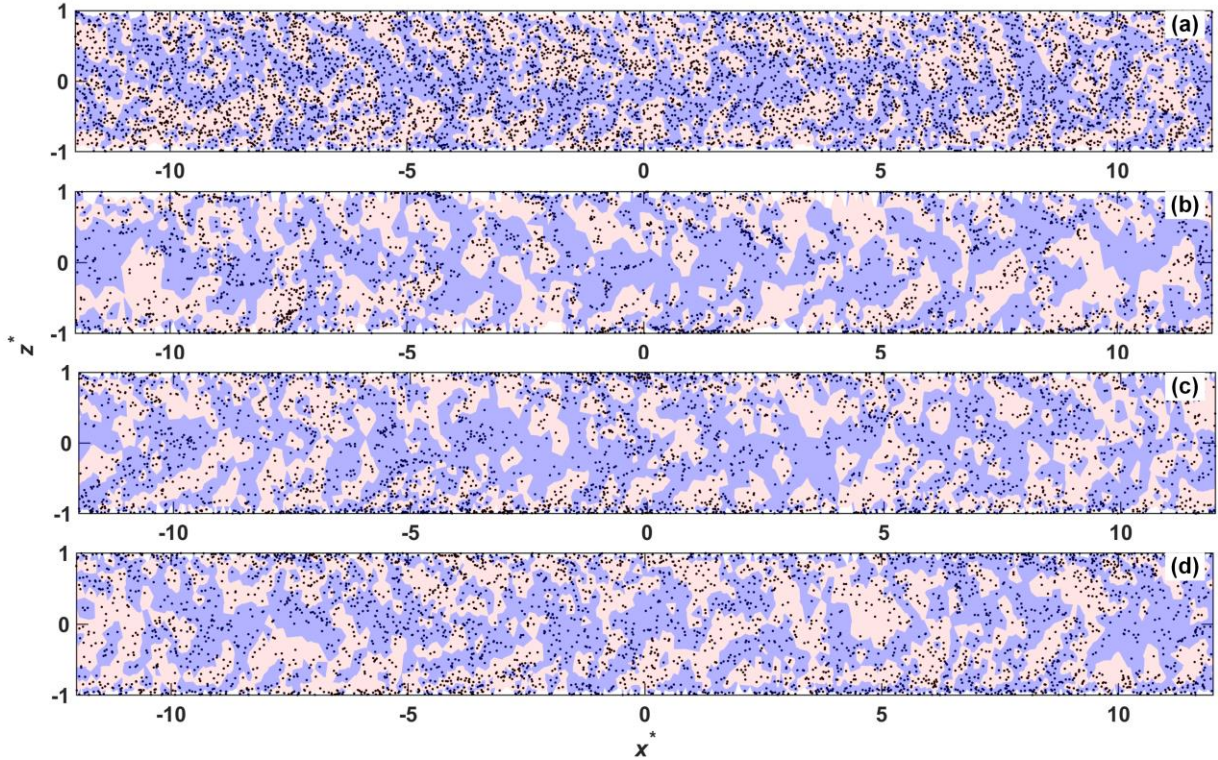

FIG. 18. Instantaneous particle distribution superimposed with the contour of instantaneous transverse fluid velocity v_f at the particle position near the free surface for all particle Stokes numbers considered: (a) St^+=0.31, (b) St^+=25, (c) St^+=125, and (d) St^+=260. The purple regions denote $v_f < 0$, while pink regions denote $v_f > 0$.

To further support the observations made in relation to Fig. 18, Fig. 19 plots the profiles of PDFs of instantaneous transverse fluid velocity computed at the locations of particle clusters for the indicated particles. Evidently, the peaks of all the PDF curves are located in the regions of $v_f < 0$. Two types of mechanism are responsible for the particle clustering near the free surface in the present open square duct flow. Firstly, particles can be entrained to the free surface by upwellings of the fluid motion, which are mainly generated by the ejection events emanating from the sidewalls as they are convected toward the free surface. After then, the light particles can leave the free surface again by following the downwellings of the same cross-sectional vortices. However, heavier particles cannot easily leave the free surface due to their high inertia, which finally leads to their accumulation in the area of downwellings. Secondly, the transverse components of the mean inner and outer secondary flow can strengthen the effects of the first mechanism. This can be verified through Fig. 13, where the magnitude of upward secondary velocity for heavier particles is much larger than that of the downward secondary velocity. Furthermore, the strong mean spanwise secondary flow along the free surface can sweep the particles from regions of high transverse fluctuations ($z^*=\pm0.8$) to the upper corner or the central regions of the free surface, where the transverse fluctuations are lower. This further results in the formation of inclined particle streaks in Fig. 18(b) and the increase in mean particle concentration in the upper corner and central region of the free surface, as shown in Fig. 7(c).
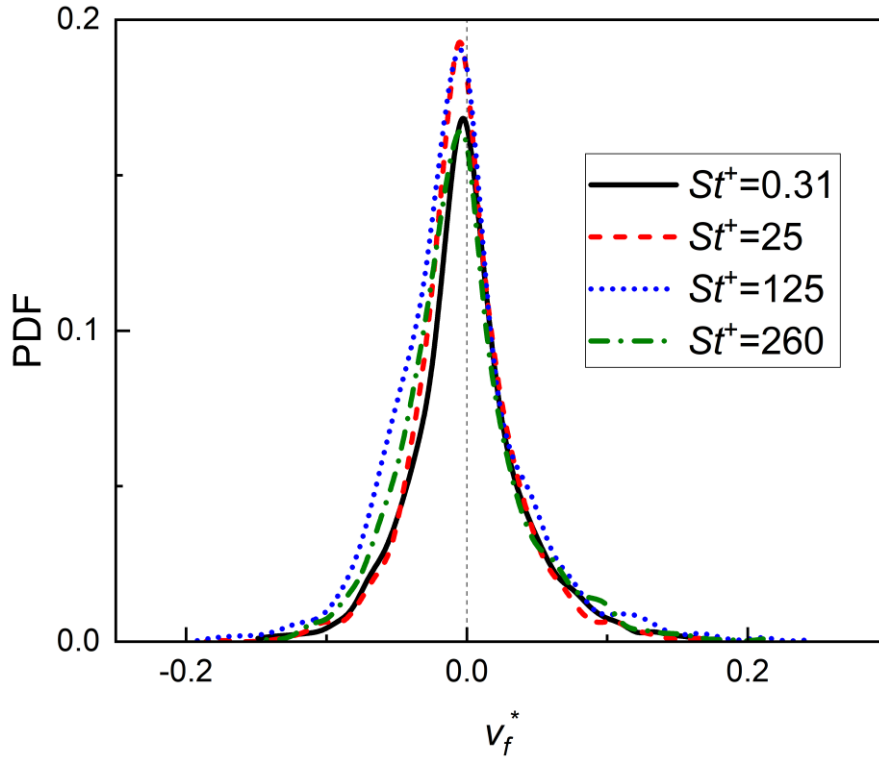

FIG. 19. PDFs of instantaneous transverse fluid velocity computed at the locations of particle clusters for all particle Stokes numbers considered.

6. Particle transport mechanism analysis

Based on the above discussion, the fundamental mechanism of particle transportation in turbulent square duct flow with a free surface can be summarized in Fig. 20. As a result of the canonical turbophoresis in wall-bounded turbulence, inertial particles are susceptible to accumulate near the sidewalls and bottom wall of the open square duct. However, the convection of cross-sectional secondary flows can transport particles from the sidewall to the free surface, which results in a lower particle concentration near the sidewall as compared to the bottom wall. Simultaneously, the particle accumulation trends in the vicinity of the wall or free surface can also be modulated by the secondary flow near these boundaries. Specifically, particles can move from the central regions of the duct cross-section towards the lower corners along the lower corner bisector, following the streamlines of outer secondary flow, which contains two vortices (referred to as vortex "A" and vortex "B" in Fig. 20). They then make a 45° turn and move along the sidewall until they reach the location where the outer and inner secondary flows meet (position "C" in Fig. 20). At this point, they make another 45° turn before moving along the free surface towards the central surface region. From there, they turn downward and return to the duct central region. During this process, as particles approach the lower duct corner, which is a stagnation region of the secondary flow (enclosed within the blue curve at the bottom corner in Fig. 20), some of the heavier particles tend to accumulate and remain there because of their high inertia. Other particles have the option to follow the upward outer secondary flow (mainly the effect of vortex "B") along the sidewall or the horizontal bottom secondary flow in order to exit the corner region. Particles that follow the bottom secondary flow away from the lower corner region are primarily influenced by the near-wall coherent structures, which causes them to accumulate in the low-fluid-speed streaks located in the middle area of the bottom wall (the region marked in gray in Fig. 20). Overall, in the lower half of the duct cross-section, the mechanisms responsible for particle motion are comparable to those in a closed duct flow [17]. For particles that leave the bottom corner and move upwards along the sidewall, their wall orientation behaviour is similar to that on the bottom wall. As the upper corners are approached, the low-inertia particles can be entrained by the inner secondary flow to the free surface, where they then move downward and return to position "C" along the sidewall. Although high-inertia particles may not be able to follow the inner secondary flow throughout the cycle, their upward motion is still somewhat suppressed by the downward inner secondary flow along the sidewall, which further leads to the accumulation of particles at position "C". In the upper half of the duct cross section, the ability of $St^+ \geq 25$ particles to follow the outer secondary vortex "A" decreases with increasing inertia. Consequently, particles with high inertia are more likely to remain close to the free surface upon reaching it, while particles with low inertia continue to follow

the secondary flow down the midline of the free surface back to the central region of the duct. Near the free surface, heavier particles tend to concentrate in the downwelling regions of fluid motion, where the streamwise and transverse flow fluctuations are relatively low. In contrast, particles located in upwellings, where flow fluctuations are higher, are easily carried or entrained to other locations by the strong outer secondary flow along the free surface.
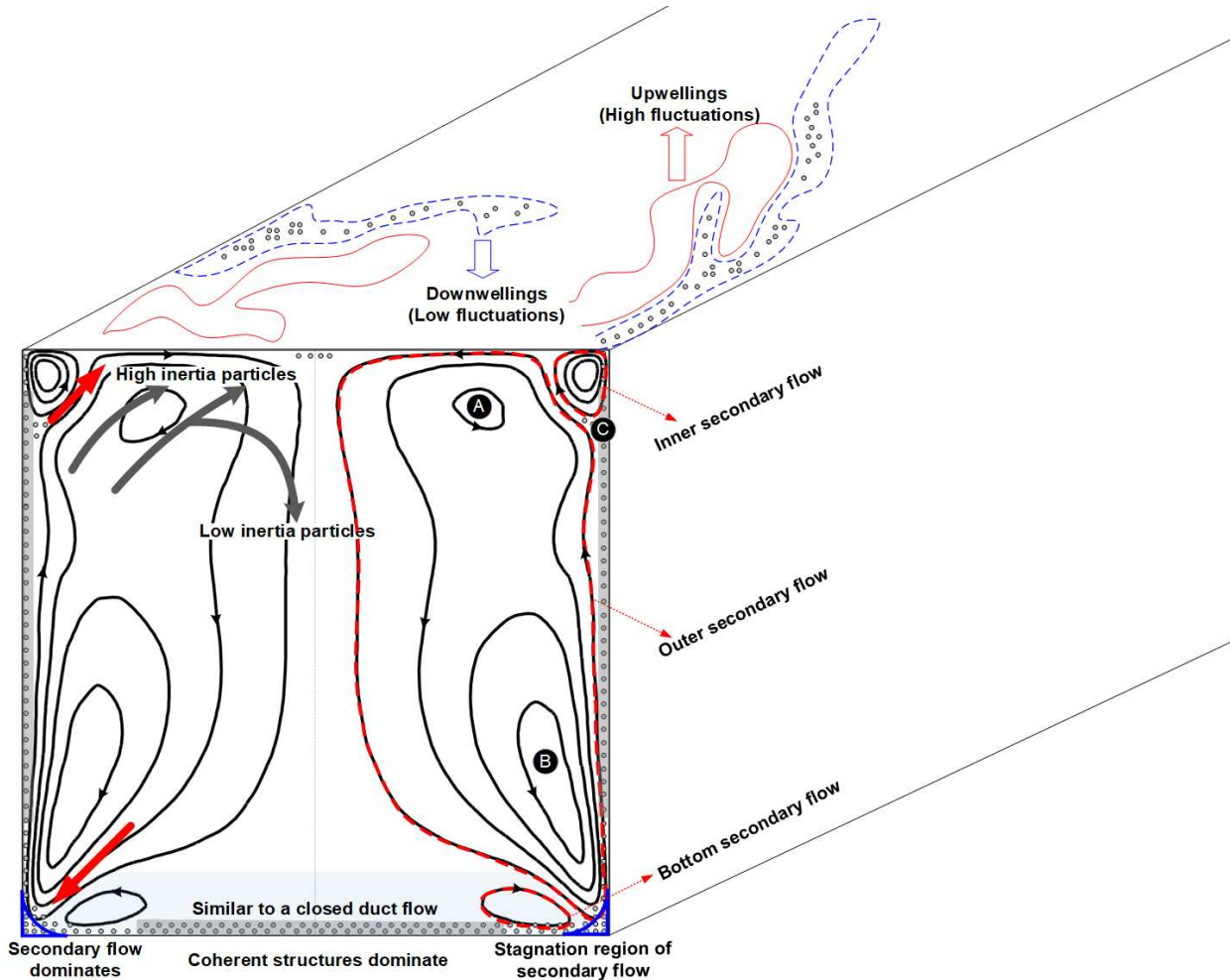

FIG. 20. Schematic illustration of particle transport in turbulent square duct flow with a free surface.

IV. CONCLUSIONS

Direct numerical simulation in combination with a one-way coupled Lagrangian particle tracking technique has been used to study turbulent particle-laden flows in a dilute open square duct with a free surface. The flow shear Reynolds number is Re_τ=300, and the shear particle Stokes numbers investigated range from St^+=0.31 to 260. The main objective was to explore the effect of cross-stream secondary flows, induced by the anisotropy of turbulence in the mixed boundary of solid wall and free surface, on particle transport in the fully turbulent open square duct.

Results obtained for the fluid phase show that the inner and outer secondary flows in the cross-sectional plane

of the open square duct are accurately predicted. Under their effect, the transverse position of the maximum streamwise velocity moves to $y^*=0.22$ under the free surface. The maximum velocity of secondary flow is achieved at the free surface, reaching 4.3% of the mean streamwise velocity, which is much larger than that observed in closed square duct flows. Unlike the canonical open channel flow, the spanwise component of $r.m.s.$ velocities at the free surface is found to be higher than the streamwise component due to the strong secondary flow there.

For the particulate phase, particles tend to accumulate near the bottom and sidewalls of the duct. However, the particle concentration near the sidewalls is lower than that near the bottom wall, which is because the mean outer secondary flows can entrain some particles from the sidewalls to the free surface. For heavier particles with $St^+ \geq 25$ in the duct cross-section, the position of the mean concentration maximum is located at the lower corners, with the highest concentration values found for $St^+=25$ particles. The minimum particle concentration is observed at the free surface. Along the bottom-wall bisector, the particle concentration generally decreases from the bottom, up to the free surface, except for close to the free surface, where the concentration slightly increases. This rebound in concentration is most pronounced for particles with $St^+=25$ and decreases in magnitude as the Stokes number increases further. In the lower half of the duct cross section, the profiles of mean particle concentration along the bottom wall and sidewall resemble those observed in closed square duct flows [17]. Approaching the upper corner along the sidewall, a local peak in particle concentration occurs at $y^*=0.75$, resulting from the combined effect of the inner and outer secondary flows in this area. Along the free surface, the concentration of particles with $St^+ \geq 25$ gradually decreases as moving away from the sidewall, while the exact opposite trend is found for $St^+=0.31$ particles. In the streamwise direction, heavier particles tend to accumulate in low-velocity streaks and form elongated coherent clusters near the sidewall and bottom wall. The maximum clustering level is observed for $St^+=25$ particles. These particles also exhibit preferential concentration near the free surface, although the concentration there is relatively low. Further analysis of particle accumulation near the free surface demonstrates that the heavier particles with $St^+ \geq 25$ tend to accumulate in regions where the instantaneous transverse secondary flow velocity is negative, with the level of accumulation decreasing as the Stokes number increases.

Contours of the mean streamwise particle velocity in the duct cross section are observed to resemble those of the fluid phase. As the Stokes number is increased, the streamwise particle velocity in the central region of the duct cross section ($-0.25<y^*<0.5$) gradually decreases. However, the opposite trend is found for the mean streamwise velocity of $St^+ \geq 25$ particles in the buffer layer near the bottom wall and in the region of $y^* > 0.75$ near the free surface along the bottom-wall bisector. Furthermore, the position of the maximum streamwise particle velocity is found to be closer to the free surface with increasing particle inertia. For the secondary motion, the distribution of $St^+=0.31$

particles in the cross-sectional plane is similar to that of the continuous phase. However, as particle inertia increases, the rotation centres of inner and outer secondary particle motions gradually disappear, and the magnitude of the corresponding secondary particle velocity decreases. In particular, there exists a change in direction of the transverse secondary velocity for $St^+\geqslant 25$ particles in the region of $y^*>-0.5$ along the bottom-wall bisector. The Stokes number dependence of secondary particle motions in the region below the lower corner bisector is analogous to that in a closed square duct flow [17], where the secondary velocity for $St^+=25$ particles is significantly enhanced along the lower corner bisector. Regarding the particle velocity fluctuations, the maxima is observed to be located close to the wall, with its proximity to the boundary reducing with increasing Stokes number. Moreover, there is a local minimum of TKE for all particles in the lower duct corner, while in the upper corner of the mixed boundary, the particle TKE increases with Stokes number. Generally, the streamwise *r.m.s.* velocities for all inertial particles are enhanced compared to the fluid phase, with a larger increase as the Stokes number increases. Interestingly, the streamwise *r.m.s.* velocity of the $St^+=0.31$ particles is found to be larger than that of the higher-inertia particles in the central area of the free surface. Furthermore, their *r.m.s.* velocities in the transverse and spanwise directions along the bottom-wall bisector are also increased. Conversely, the transverse and spanwise *r.m.s.* velocities for $St^+\geq 25$ particles are largely suppressed.

Particle-induced effects on wall-bounded turbulence must be considered when the particle volume fraction is relatively high. Previous studies [15,16] have shown that the presence of large buoyant particles can enhance the cross-sectional secondary flow in a closed duct flow, with this enhancement effect intensified with increasing particle volume fraction until a certain saturation value is achieved. In addition, deformation of the free surface due to the fluid gravity is also expected to have a large impact on the distribution of the secondary flow near the free surface in an open channel flow [52]. Therefore, it is essential to further investigate particle-laden flows in turbulent open square ducts with higher particle concentrations, considering two-way coupling effects and surface deformation. Future studies should aim to explore these aspects to gain a more comprehensive understanding of the particle behaviour and its effects on the flow dynamics in such systems.

ACKNOWLEDGMENTS

of Association for Science and Technology in Yanan, China.

DATA AVAILABILITY

The data that support the findings of this study are available from the corresponding author upon reasonable request.

REFERENCES

1. K. Alba, "Colloidal exchange flow in ducts," J. Fluid Mech. A9, 942 (2022).

2. Z. Sun, J. Al Salami, A. Khodak, F. Saenz, B. Wynne, R. Maingi, and E. Kolemen, "Magnetohydrodynamics in free surface liquid metal flow relevant to plasma-facing components," Nucl. Fusion 63, 076022(2023).

3. A. Kumar, S. Sen, S. Hossain, and K. Ghoshal, "Unsteady two-dimensional distribution of suspended sediment transport in open channels," Environ Fluid Mech., (2023). https://doi.org/10.1007/s10652-023-09933-1.

4. A. Tominaga, I. Nezu, K. Ezaki, and H. Nakagawa, "Three-dimensional turbulent structure in straight open channel flows," J. Hydraul. Res. 27, 149 (1989).

5. R. B. Roglia, A. P. Ascarelli, and U. Piomelli, "Large-eddy simulation of ducts with a free surface," J. Fluid Mech. 484, 223 (2003).

6. D. Demiral, R. M. Boes, and I. Albayrak, "Effects of secondary currents on turbulence characteristics of supercritical open channel flows at low aspect ratios," Water 12, 3233(2020).

7. F. Gessner, "The origin of secondary flow in turbulent flow along a corner," J. Fluid Mech. 58, 1 (1973).

8. A. Huser and S. Biringen, "Direct numerical simulation of turbulent flow in a square duct," J. Fluid Mech. 257, 65 (1993).

9. A. Pinelli, M. Uhlmann, A. Sekimoto, and G. Kawahara, "Reynolds number dependence of mean flow structure in square duct turbulence," J. Fluid Mech. 644, 107 (2010).

10. S. Pirozzoli, D. Modesti, P. Orlandi, and F. Grasso, "Turbulence and secondary motions in square duct flow," J. Fluid Mech. 840, 631 (2018).

11. C. M. Winkler, S. L. Rani, and S. P. Vanka, "A numerical study of particle wall-deposition in a turbulent square duct flow," Powder Technol. 170, 12 (2006).

12. D. J. Phares, and G. Sharma, "A DNS Study of aerosol deposition in a turbulent square duct flow," Aerosol Sci. Technol. 40, 1016 (2006).

13. J. Yao and M. Fairweather, "Particle deposition in turbulent duct flows," Chem. Eng. Sci. 84, 781 (2012).

14. A. Noorani, R. Vinuesa, L. Brandt, and P. Schlatter, "Aspect ratio effect on particle transport in turbulent duct flows," Phys. Fluids 28, 115103 (2016)

15. Z. Lin, Z. Yu, X. Shao, and L.-P. Wang, "Effects of finite-size neutrally buoyant particles on the turbulent flows in a square duct," Phys. Fluids 29, 103304 (2017)

16. W. Fornari, H. T. Kazerooni, J. Hussong, and L. Brandt, "Suspensions of finite-size neutrally buoyant spheres in turbulent duct flow," J. Fluid Mech. 851, 148 (2018).

17. Y. Wang, M. Fairweather, L. F. Mortimer, Y. Zhao, and J. Yao, "Mechanisms of particle preferential concentration induced by secondary motions in a dilute turbulent square duct flow," Phys. Fluids 32, 123313 (2020).

18. L. M. Grega, T. Wei, R. I. Leighton, and J. C. Neves, "Turbulent mixed-boundary flow in a corner formed by a solid wall and a free surface," J. Fluid Mech. 294, 17 (1995).

19. M. Sreedhar, and F. Stern, "Large eddy simulation of temporally developing juncture flows," Int. J. Numer. Meth. Fl. 28, 47 (1998).

20. H. Kang, and S. U. Choi, "Reynolds stress modelling of rectangular open-channel flow," Int. J. Numer. Meth. Fl. 51, 1319 (2006).

21. Y. Sakai, and M. Uhlmann, "High-resolution numerical analysis of turbulent flow in straight ducts with rectangular cross-section," In: Nagel, W., Kröner, D., Resch, M. (eds) High Performance Computing in Science and Engineering '15. Springer, Cham. (2016). https://doi.org/10.1007/978-3-319-24633-8_20.

22. N. Nikitin, "Turbulent secondary flows in channels with no-slip and shear-free boundaries," J. Fluid Mech. 917, A24 (2021).

23. C. Narayanan, D. Lakehal, L. Botto, and A. Soldati, "Mechanisms of particle deposition in a fully developed turbulent open channel flow," Phys. Fluids 3, 15 (2003).

24. A. G. Kidanemariam, C. Chan-Braun, T. Doychev, and M. Uhlmann, "Direct numerical simulation of horizontal open channel flow with finite-size, heavy particles at low solid volume fraction," New J. Phys. 15, 025031 (2013).

25. Y. Wang, and K. M. Lam, "Clustering behaviour and settling velocity of bidisperse inertial particles in turbulent open channel flow," Int. J. Multiphase Flow 129, 103303 (2020).

26. B. van Haarlem, B. J. Boersma, and F. T. M. Nieuwstadt, "Direct numerical simulation of particle deposition onto a free-slip and no-slip surface," Phys. Fluids 10, 2608 (1998).

27. S. Lovecchio, C. Marchioli, and A. Soldati, "Time persistence of floating-particle clusters in free-surface turbulence," Phys. Rev. E 88, 033003 (2013).

28. S. Kundu, and K. Ghoshal, "Effects of secondary current and stratification on suspension concentration in an open channel flow," Environ. Fluid Mech. 14, 1357 (2014).

29. Y. Wang, Y. Zhao, and J. Yao, "Particle dispersion in turbulent, square open duct flows of high Reynolds number," Powder Technol. 354, 92 (2019).

30. S. Gavrilakis, "Numerical simulation of low-Reynolds-number turbulent flow through a straight square duct," J. Fluid Mech. 244, 101 (1992).

31. M. Uhlmann, A. Pinelli, G. Kawahara, and A. Sekimoto, "Marginally turbulent flow in a square duct," J. Fluid Mech. 588, 153 (2007).

32. H. Zhang, F. X. Trias, A. Gorobets, Y. Tan, and A. Oliva, "Direct numerical simulation of a fully developed turbulent square duct flow up to Re_τ=1200," Int. J. Heat Fluid Fl. 54, 258 (2015).

33. P. F. Fischer, J. W. Lottes, and S. G. Kerkemeier, Nek5000, http://nek5000.mcs.anl.gov, 2008.

34. A.W. Vreman, J.G.M. Kuerten, "Comparison of direct numerical simulation databases of turbulent channel flow at $Re\tau$=180," Phys. Fluids 26, 015102 (2014).

35. R. Vinuesa, A. Noorani, A. Lozano-Durán, G. K. E. Khoury, P. Schlatter, P. F. Fischer, and H. M. Nagib, "Aspect ratio effects in turbulent duct flows studied through direct numerical simulation," J. Turbul. 15, 677 (2014).

36. P. Bagchi and S. Balachandar. "Effect of turbulence on the drag and lift of a particle," Phys. Fluids 15, 3496 (2003).

37. C. Jin, I. Potts, and M. W. Reeks, "The effects of near wall corrections to hydrodynamic forces on particle deposition and transport in vertical turbulent boundary layers," Int. J. Multiphase Flow 79, 62 (2016).

38. Y. Yan, Y. Zhao, J. Yao, and C. H. Wang, "Investigation of particle transport by a turbulent flow through a 90° bend pipe with electrostatic effects," Powder Technol. 394, 547(2021).

39. Y. Yan, Y. Zhao, M. Liu, and J. Yao, "Reynolds number dependence of particle transport in a 90° bend with electrostatic effects," Particuology 77, 91(2023).

40. Y. Pan and S. Banerjee, "Numerical simulation of particle interactions with wall turbulence," Phys. Fluids 8, 2733 (1996).

41. A. Daitche, "On the role of the history force for inertial particles in turbulence," J. Fluid Mech. 782, 567 (2015).

42. V. Armenio and V. Fiorotto, "The importance of the forces acting on particles in turbulent flows," Phys. Fluids 13, 2437 (2001).

43. J. Shi, T.G. Thomas, and J.J.R. Williams, "Large-eddy simulation of flow in a rectangular open channel," J. Hydraul. Res. 37, 345 (1999).

44. L. F. Mortimer, D.O. Njobuenwu, and M. Fairweather, "Near-wall dynamics of inertial particles in dilute turbulent channel flows," Phys. Fluids 31, 063302 (2019).

45. C. Nilsen, H. I. Andersson, and L. Zhao, "A Voronoï analysis of preferential concentration in a vertical channel flow," Phys. Fluids 25, 115108 (2013).

46. A. Soldati, and C. Marchioli, "Sediment transport in steady turbulent boundary layers: Potentials, limitations, and perspectives for Lagrangian tracking in DNS and LES," Adv. Water Resour. 48, 18 (2012).

47. A. Soldati, and C. Marchioli, "Physics and modelling of turbulent particle deposition and entrainment: Review of a systematic

study," Int. J. Multiphase Flow 35, 827 (2009).

48. Y. Joung, S. U. Choi, and J. I. Choi, "Direct numerical simulation of turbulent flow in a square duct: analysis of secondary flows," J. Eng. Mech.133, 213 (2007).

49. M. Picciotto, C. Marchioli, M. W. Reeks, and A. Soldati, "Statistics of velocity and preferential accumulation of micro-particles in boundary layer turbulence," Nucl. Eng. Des. 235, 1239 (2005).

50. L. M. Portela, P. Cota, and R. V. A. Oliemans, "Numerical study of the near-wall behaviour of particles in turbulent pipe flows," Powder Technol. 125, 149 (2002).

51. S. Lovecchio, F. Zonta, and A. Soldati, "Influence of thermal stratification on the surfacing and clustering of floaters in free surface turbulence," Adv. Water Resour. 2, 22 (2014).

52. S. Smolentsev and R. Miraghaie, "Study of a free surface in open-channel water flows in the regime from "weak" to "strong" turbulence," Int. J. Multiphase Flow 31, 921 (2005).